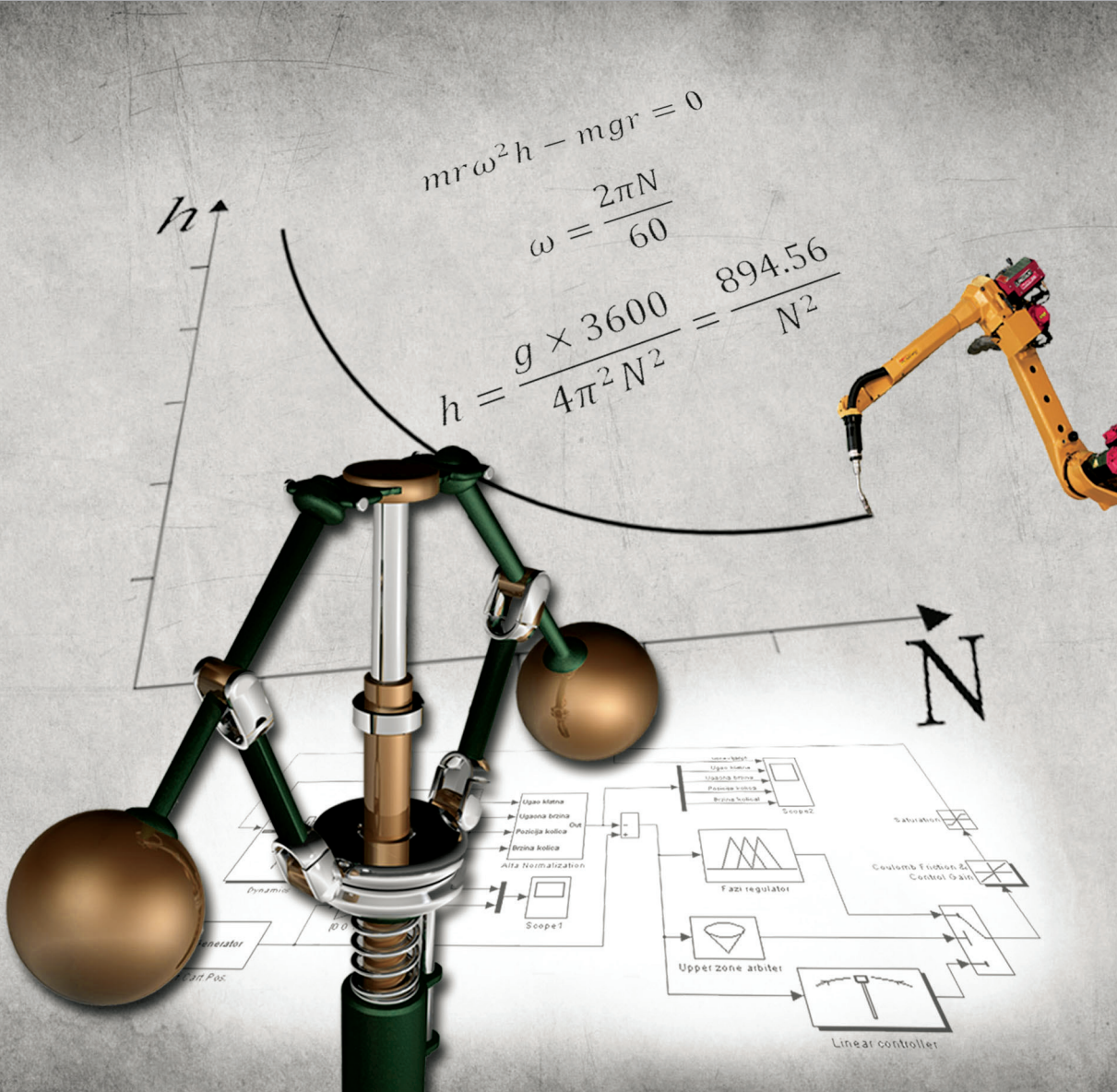




FACTA UNIVERSITATIS

Series
AUTOMATIC CONTROL AND ROBOTICS
Vol. 21, № 2, 2022



Scientific Journal **FACTA UNIVERSITATIS**
UNIVERSITY OF NIŠ

Univerzitetski trg 2, 18000 Niš, Republic of Serbia

Phone: +381 18 257 095 Telefax: +381 18 257 950

e-mail: facta@ni.ac.rs <http://casopisi.junis.ni.ac.rs/>

Scientific Journal FACTA UNIVERSITATIS publishes original high scientific level works in the fields classified accordingly into the following periodical and independent series:

<i>Architecture and Civil Engineering</i>	<i>Linguistics and Literature</i>	<i>Physical Education and Sport</i>
<i>Automatic Control and Robotics</i>	<i>Mathematics and Informatics</i>	<i>Physics, Chemistry and Technology</i>
<i>Economics and Organization</i>	<i>Mechanical Engineering</i>	<i>Teaching, Learning and Teacher Education</i>
<i>Electronics and Energetics</i>	<i>Medicine and Biology</i>	<i>Visual Arts and Music</i>
<i>Law and Politics</i>	<i>Philosophy, Sociology, Psychology and History</i>	<i>Working and Living Environmental Protection</i>

SERIES: AUTOMATIC CONTROL AND ROBOTICS

Editor-in-Chief: **Marko Milojković**, e-mail: fuacred@junis.ni.ac.rs
University of Niš, Faculty of Electronic Engineering
Republic of Serbia, 18000 Niš, Aleksandra Medvedeva 14
Phone: +381 18 529 363, Fax: +381 18 588 399

Technical Assistance: **Staniša Lj. Perić**, University of Niš, Faculty of Electronic Engineering,
Department of Control Systems, Niš, Republic of Serbia, e-mail: fuacrts@junis.ni.ac.rs

EDITORIAL BOARD:

Dragan Antić,

Faculty of Electronic Engineering,
University of Niš, Republic of Serbia

Branko Kovačević,

Faculty of Electrical Engineering,
University of Belgrade, Republic of Serbia

Emil Nikolov,

Faculty of Automatics,
Technical University of Sofia, Bulgaria

Stevan Stankovski,

Faculty of Technical Sciences,
University of Novi Sad, Republic of Serbia

Žarko Čučej,

Faculty of Electrical Engineering and Computer
Science, University of Maribor, Slovenia

Viacheslav Khasanovich Pshikhopov,

Head of the Electrical Engineering and
Mechatronics, Department Taganrog Technological
Institute Southern Federal University, Russia

Milić Stojić,

School of Electrical Engineering,
University of Belgrade, Republic of Serbia

Radu-Emil Precup,

Faculty of Automation and Computers,
"Politehnica" University of Timisoara, Romania

Branislav Borovac,

Faculty of Technical Sciences,
University of Novi Sad, Republic of Serbia

Mile Stankovski,

Faculty of Electrical Engineering and Information Technology,
Skopje, Macedonia

Georgi Dimirovski,

School of Engineering,
Dogus University, Istanbul, Republic of Turkey

Morten Hovd,

Norwegian University of Science and Technology, Trondheim,
Norway

Vlastimir Nikolić,

Faculty of Mechanical Engineering,
University of Niš, Republic of Serbia

Željko Đurović,

School of Electrical Engineering,
University of Belgrade, Republic of Serbia

Zoran Bučevac,

Faculty of Mechanical Engineering,
University of Belgrade, Republic of Serbia

Novak Nedić,

Faculty of Mechanical Engineering Kraljevo,
University of Kragujevac, Republic of Serbia

UDC Classification Associate: **Branka Stanković**, Library of Faculty of Electronic Engineering, Niš

English Proofreader: **Goran Stevanović**, University of Niš, Faculty of Civil Engineering and Architecture, e-mail: fuacrpr@junis.ni.ac.rs

The authors themselves are responsible for the correctness of the English language in the body of papers.

Secretary: **Olgica Davidović**, University of Niš, e-mail: olgicad@ni.ac.rs

Computer support: **Mile Ž. Randelović**, University of Niš, e-mail: mile@ni.ac.rs

Publication frequency – one volume, three issues per year.

Published by the University of Niš, Republic of Serbia

© 2022 by University of Niš, Republic of Serbia

Financial support: Ministry of Education, Science and Technological Development of the Republic of Serbia

Printed by ATLANTIS DOO, Niš, Republic of Serbia

Circulation 60

Previous title: Scientific Journal FACTA UNIVERSITATIS, Series Mechanics, Automatic Control and Robotics. – Vol. 1, No 1 (1991) – Vol. 6, No 1(2007). – ISSN 0354 – 2009

Since 2007 divided in two Series:

Scientific Journal FACTA UNIVERSITATIS, Series Mechanics. – Vol. 7, No 1(2008) – . – ISSN

Scientific Journal FACTA UNIVERSITATIS, Series Automatic Control and Robotics. – Vol. 7, No 1(2008) – . – ISSN 1820 – 6417

ISSN 1820 – 6417 (Print)
ISSN 1820 – 6425 (Online)
COBISS.SR-ID 158108940
UDC 62

FACTA UNIVERSITATIS

SERIES AUTOMATIC CONTROL AND ROBOTICS
Vol. 21, № 2, 2022



UNIVERSITY OF NIŠ

INSTRUCTION FOR AUTHORS

As an author, you are kindly advised to use the paper template available for downloading on journal web site (section Download documents). This way you have nothing to change in terms of paper and text format. Simply applying the styles defined in the document will be sufficient.

Paper submitted for publication may be written in English, French or German (preferably in English) and submitted in the final camera-ready form. It is mandatory to submit your original work in Microsoft Word format (.doc not .docx) by using our online manuscript submission system. You have to make "New Submission" and upload your paper by using the online interface. All subsequent versions should be uploaded by using the same paper ID and your defined password. We are unable to process files sent by E-mail. We will do the final formatting and all necessary format conversions of your paper.

Articles are usually 10 to 25 type-written pages long. However, in special cases, shorter or longer articles may be accepted with appropriate reasoning. Author name, affiliation and complete address are to be placed underneath the title. Each paper should be preceded by a brief summary (50-150 words) in the same language. The text should be concise.

Letters, figures, and symbols should be clearly denoted so that no doubts about their meaning can arise. Symbols which may lead to confusion (e.g. letter I and figure 1, figure 0 and letter O) should be distinguished by marks which are explained in "Remarks for the typesetter".

Equations should be typewritten using MathType add-on (<http://www.mathtype.com>). For equations in your paper (Insert | Object | Create New | or MathType Equation), and, with the number, placed in parentheses at the right margin. Reference to equations should use the form "Eq. (2)" or simply (2). Each formula should occupy one line.

All figures should be numbered with consecutive Arabic numbers, have descriptive captions, and be mentioned in the text. Figures submitted must be of a standard high enough for direct reproduction. Line drawings should be prepared in electronic form. Figures should be planned in advance, so as to allow reduction to 12.75 cm in column width.

References should be quoted in the text by the corresponding number in square brackets and listed at the end of the manuscript in the order as they shown in the paper, in the same way as the following examples (for a journal, book, unpublished paper, proceeding, thesis, user manual, internet document):

- [1] B. M. Danković, "A class of almost orthogonal filters," *Journal of Circuits, Systems, and Computers*, vol. 18, no. 5, pp. 923–931, 2009. [Online]. Available: <http://dx.doi.org/10.1142/S0218126609005447>
- [2] J. H. Holland, *Adaptation in Natural and Artificial Systems*. University of Michigan Press, Ann Arbor, 1975.
- [3] M. T. Milojković, D. S. Antić, S. S. Nikolić, Z. D. Jovanović, S. Lj. Perić, "On a new class of quasi-orthogonal filters," *International Journal of Electronics*, [Online]. Available: <http://dx.doi.org/10.1080/00207217.2012.743087>, to be published.
- [4] M.-B. Radac, R.-A. Achimescu, R.-E. Precup, S. Preitl, C.-A. Dragos, A.-I. Stinean, "Design and experiments for model-free PI control of DC drives," in *Proceedings of 8th IEEE International Symposium on Applied Computational Intelligence and Informatics*, Timisoara, Romania, pp. 103–108, 2013. [Online]. Available: <http://dx.doi.org/10.1225/sc.2013.018>
- [5] D. Mitić, Digital variable structure systems based on input-output model. PhD thesis, University of Niš, Faculty of Electronic Engineering, 2006.
- [6] Inteco, "The laboratory anti-lock braking system controlled from PC," User's manual, 2008. [Online]. Available: www.inteco.com.pl
- [7] MATLAB, The Language of Technical Computing, 2013. [Online]. Available: <http://www.mathworks.com/products/matlab> [Accessed on December 2013].

Electronic submission. Papers for consideration should be submitted to the Series Editor in electronic form via the Journal's home page: <http://casopisi.junis.ni.ac.rs/index.php/FUAutContRob/index>.

FACTA UNIVERSITATIS

Series

Automatic Control and Robotics

Vol. 21, N° 2, 2022

Contents

Regular Papers

Ivana Rogan, Olivera Pronić-Rančić

COMBINED TECHNIQUES FOR FORECASTING THE VOLUME OF PACKAGES
IN INTERNAL POSTAL TRAFFIC OF SERBIA..... 59-75

Saša S. Nikolić, Igor Kocić, Dragan Antić, Darko Mitić,

Nikola Danković, Aleksandra Milovanović, Petar Đekić

THE WINDER DANCER POSITION CONTROL MODEL
USING DIFFERENT PID CONTROL STRUCTURES AND MICROLOGIX PLC 77-93

Milan Dinčić, Zoran Perić, Dragan Denić

OPTIMIZATION AND PERFORMANCE ANALYSIS
OF THE 30-BIT FIXED-POINT DIGITAL FORMAT 95-105

Veljko Stanković, Zoran Perić

OFDM LOW COMPLEXITY CHANNEL ESTIMATION
USING TIME-FREQUENCY ADJUSTABLE WINDOW FUNCTIONS 107-116

Jelena Anastasov, Aleksandra Panajotović, Dejan Milić, Daniela Milović

PERFORMANCE OF SECURE COMMUNICATION
OVER α -FISHER-SNEDECOR FADING CHANNELS 117-130

COMBINED TECHNIQUES FOR FORECASTING THE VOLUME OF PACKAGES IN INTERNAL POSTAL TRAFFIC OF SERBIA

UDC ((621.391+004.032.26):656.8)

Ivana Rogan, Olivera Pronić-Rančić

University of Niš, Faculty of Electronic Engineering,
Department of Telecommunications, Niš, Republic of Serbia

Abstract. *The main goal of time series analysis is to explain the main features of the data in a chronological order and in the general case to predict future processes, products, service requirements, etc., using appropriate statistical models. In this paper, time series prediction was performed using a seasonal autoregressive integrated moving average model (SARIMA) in the XLSTAT add-in for Excel environment, as well as two artificial neural network (ANN) models - long short-term memory (LSTM) network and relatively new machine learning technique - extreme learning machines (ELM). The proposed approaches were used for forecasting the volume of packages in the internal postal traffic of Serbia for the period 2014-2020. A comparison of the obtained modeling results with the original data was made and it was shown that the best modelling results were achieved by using ELM.*

Key words: *Time series analysis, forecasting, ANN, SARIMA, LSTM, ELM*

1. INTRODUCTION

A time series is a sequence of observations of a random, here, real, non-negative, variables. Time series analysis provides tools, mostly of the essential, statistical and/or analytical-approximate type, to select a model that can be used to anticipate future events. In this context, predicting future values is an appropriate mathematical method for extrapolating future data, depending on external influences and chronologically arranged numerical information, [1-7].

In cases of time series data prediction, several different techniques have been applied, [1-22]. Theoretical, general, and special techniques and softwares for numerical prediction

Received March 30, 2022 / Accepted June 16, 2022

Corresponding author: Ivana Rogan

University of Niš, Faculty of Electronic Engineering, Department of Telecommunications,

Aleksandra Medvedeva 14, 18000 Niš, Republic of Serbia

E-mail: ivana84p@gmail.com

were presented in [1-7]. For example, [4] provides a modern overview of a broad range of methods, principles, and theoretical approaches to prepare, produce, organize, and evaluate forecasts. Concrete hybrid models, deterministic, (S)ARIMA with Artificial Neural Networks (ANN) were presented in [8] and, in [9], integration of EWT (Empirical Wavelet Transform), ARIMA with the improved ABC Optimized ELM was proposed for financial time series forecasting. In [11], [12] MATLAB machine learning (ML) and deep learning models (among others, LSTM (Long Short-Term Memory) and ELM (Extreme Learning Machines)) were considered. The directions of development of LSTM methods were observed in [13-17]. The properties and variations of ELM technique were shown in [18-24].

Forecasting the revenue and volume of some postal services is presented in [27-29]. Savitzky-Golay filter modification for forecasting the volume of postal services was presented in [28]. In [29] time series analysis techniques based on the SARIMA model, as well as the LSTM model, for predicting the volume of received express mail services in international traffic in the Republic of Serbia were developed. A bias correction to the minimum Akaike information criterion, AIC, is derived for regression and autoregressive time series models in [30].

In this paper, we will consider different techniques for forecasting the volume of packages in the internal postal traffic in Serbia. Parcel Services of the Post of Serbia are used to transfer goods and other items. A parcel is a closed postal item containing goods and other items, with or without indicated value, with registered reception number, [31]. The aim of the paper is to introduce new ANN methods, due to expected better results, into the methodology of forecasting the volume of packages in the Serbian internal postal traffic and thus contribute to more adequate or automated decision-making in relation to them. Time series prediction will be performed using a seasonal autoregressive integrated moving average model (SARIMA) in the XLSTAT add-in for Excel environment, as well as two ANN models - long short-term memory (LSTM) network and extreme learning machines (ELM).

The paper is organized as follows. After Introduction, a brief description of used forecasting models is given in Section 2. The most illustrative numerical results are presented in Section 3, and finally conclusion remarks are given in Section 4.

2. FORECASTING MODELS

In this paper, we considered several techniques for time series data forecasting: SARIMA, LSTM and ELM.

a) SARIMA

ARIMA [5] is basically a linear model assuming that time series data is stationary. Therefore, there is a limited ability to capture nonlinearities and non-stationarities in the data. ARIMA models effectively consider the serial linear correlation among observations, whereas Seasonal AutoRegressive Integrated Moving Average (SARIMA) models can satisfactorily describe time series that exhibits simple periodic non-stationarity both within and across seasons, [5]. The SARIMA approach to modeling was introduced as a statistical method of choice in the case of data derived from observations collected over a sufficiently long period of time.

ARIMA(p,d,q)(P,D,Q)_s or SARIMA models [5], are usually used when the time series has short-term correlations, trend or seasonality. The time series function $y_t = y(t)$ is defined as:

$$y_t : \{1, 2, \dots, n\} \rightarrow R^+ \cup \{0\}. \tag{1}$$

An observable time series y_t in which successive values are highly dependent can frequently be regarded as generated from a series of independent variations a_t - random deviations from normal distribution, having mean equals zero and variance σ_a^2 .

For time shift operator, B , ($B^s y_t = y_{t-s}$, $s = 0, 1, 2, \dots$), a differential linear operator, ∇ , is defined as follows: $\nabla y_t = (1 - B)y_t$.

The basic relation describing the SARIMA model is [5]:

$$\varphi_p(B) \delta_p(B^s) \nabla^d (1 - B^s)^D y_t = \mu + \chi_Q(B^s) \theta_q(B) a_t, \tag{2}$$

where

$$\varphi_p(B) = 1 - \varphi_1 B - \dots - \varphi_p B^p, \tag{3}$$

$$\theta_q(B) = 1 - \theta_1 B - \dots - \theta_q B^q, \tag{4}$$

$$\delta_p(B^s) = 1 - \delta_1 B^s - \dots - \delta_p B^{sp}, \tag{5}$$

$$\chi_Q(B) = 1 - \chi_1 B^s - \dots - \chi_Q B^{sQ}. \tag{6}$$

In equations (2) – (6), constants d and D indicate the degrees of non-seasonal and seasonal differences, s represents the seasonal time shift, and μ is the trend component. In previous equations, $\delta_1, \dots, \delta_p$ and ϕ_1, \dots, ϕ_p are seasonal and non-seasonal autoregressive constant parameters (p and P are adequate constant autoregressive parameters); χ_1, \dots, χ_Q and $\theta_1, \dots, \theta_q$ - represent seasonal and non-seasonal constant parameters of the moving averages (q and Q are adequate constant moving averages parameters), respectively. AR(p , P) - autoregressive part (p -seasonal, P -non-seasonal indexes) refers to relationship between the data variable y_t with its own lagged values. Parameter values p and P are derived from PACF (partial autocorrelation function) plots. Integrated part I(d , D) refers to order of differencing and it is essential when the series is non-stationary. In ARIMA model, Moving Average order MA(q , Q) indicates the dependence of present value of the time series variable on the lagged error terms. The order of MA part can be inferred from the Auto-Correlation Function (ACF) plot.

The (S)ARIMA model is usually treated by a three-stage iterative procedure based on identification, assessment-estimation, and diagnostic verification [4-6]. Identification generally means using all information about how batch-data is generated; assessment means the efficient use of data in order to determine the conclusions about the model parameters by the adequacy of the chosen model; and diagnostic verification means the verification of this model against data with the intent to detect any inadequacies and to make improvements to the model (**Fig 1**). ACF and PACF are often used in the identification.

The autocorrelation function (ACF) of series y_t at lag k (r_k) is, [5]

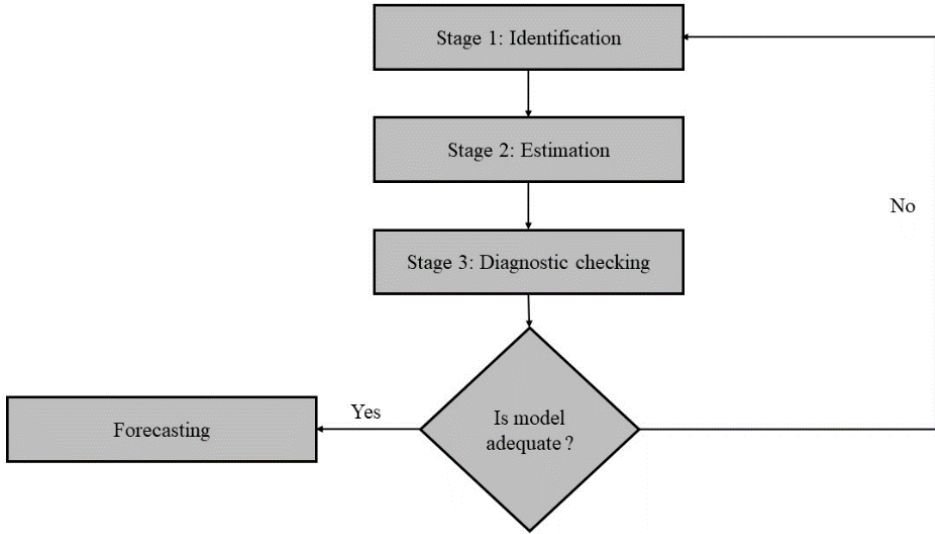


Fig. 1 Three stage of the Box-Jenkins methodology [2].

$$r_k := \frac{E[(y_t - \mu)(y_{t+k} - \mu)]}{\sigma_y^2}, \quad (7)$$

where μ is the mean value of the series, and the variance σ_y^2 of the stochastic process can be estimated by $\sigma_y^2 = \sum_{t=1}^n (y_t - \mu)^2 / n$.

The partial autocorrelation function (PACF) of series y_t at lag k (f_{kk}) is, [5]

$$f_{kk} := \begin{cases} r_{1\dots k} & k = 1; \\ \frac{r_k - \sum_{j=1}^{k-1} f_{k-1j} r_{k-1j}}{1 - \sum_{j=1}^{k-1} f_{k-1j} r_{k-1j}}, \dots & k = 2, 3, \dots, \end{cases} \quad (8)$$

where $f_{kj} = f_{k-1j} - f_{kk} f_{k-1k-j}$.

For a complete understanding of the estimation situation, it is necessary to make a thorough analytical study of the likelihood probability function. In addition, as the ACF and the PACF determine more than one model, the Akaike Information Criteria (AIC) is used to identify the best fitted model among them [5]

$$AIC = -2\ln(L(\hat{\beta})) + 2\omega, \quad (9)$$

where ω is the number of estimated parameters, and $\hat{\beta}$ is the maximum likelihood function values. AIC consists of two parts. The first item reflects the model precision and the second marks the number of model parameters, which presents a positive relation with the order number. Akaike's Small Sample Correction Information Criterion (AICC) is one of the best criteria for selecting SARIMA models, AICC is the smallest and has a

negative value. In practice, the AICC gives the best model when it has the lowest per module, a negative value.

The Q -statistics test is applied to verify the tentative adequateness of the model

$$Q = N \sum_{k=1}^m \hat{r}_k^2 \approx \chi^2(m) \quad (10)$$

where m is the specified delay lags, and N is the length of the residuals. If the calculated value of Q exceeds the critical value of $\chi^2(m)$ (m - degrees of freedom obtained from the chi-square tables), the tentative model is tuned as inadequate; otherwise, the model is adequate.

b) LSTM

Deep (structured) learning [11], [12], [17], is a subfield of machine learning methods, which is essentially a neural network with three or more layers. There are supervised, semi-supervised or unsupervised deep learning networks. ANN with a single layer can still make approximate predictions, and then additional hidden layers can aid to optimize accuracy. Deep-learning architectures in general speaking, exists as include Restricted Boltzmann Machine (RBM) based deep belief network (DBN), Convolutional Neural Network (CNN), deep Auto-encoders, and deep Recurrent Neural Network (RNN) [4], [11], [17]. In contrast to Feedforward Neural Networks, which only pass data forward, RNN have returning connections which enable using the old cell state in addition to new cell input. Hence, it can be said that the neural network has some form of memory and output at any given time is based on new and past input. As time steps pass, the influence of older inputs fades, which is why more recent inputs affect output more than older ones. However, RNNs suffer from the Vanishing Gradient problem, i. e. due to the multiplying of a large number of small values, the gradient can become a very small value [4], [12], [17]. An RNN using LSTM units can be trained in a supervised shape, on a set of training series, using an optimization algorithm, like gradient descent, combined with backpropagation through time to compute the gradients needed during the optimization process, in order to change each weight of the LSTM network in proportion to the derivative of the error (at the output layer of the LSTM network) with respect to corresponding weight. A problem with using gradient descent for standard RNNs is that error gradients vanish exponentially quickly with the size of the time lag between important events. This is due to $\lim_{n \rightarrow \infty} W_n = 0$ if the spectral radius of W -weighted matrices, is smaller than 1. However, with LSTM units, when error values are back-propagated from the output layer, the error remains in the LSTM unit's cell. This error propagating process continuously feeds error back to each of the LSTM unit's gates, until they learn to cut off the value. The main advantage of LSTM neural networks is the ability to store long-term dependencies in data [14].

LSTM used in the field of deep learning, is an artificial recurrent neural network (RNN) architecture [4], [12], [14], [17]. A frequent LSTM unit is composed of an input gate, an output gate, a cell and a forget gate. Every cell remembers values over arbitrary time intervals, the three gates regulate the flow of information into and out of the neuron. The LSTM neuron provides nonlinear mechanism for controlling the information flow into and out of the LSTM cell. The LSTM architecture is depicted in Fig. 2.

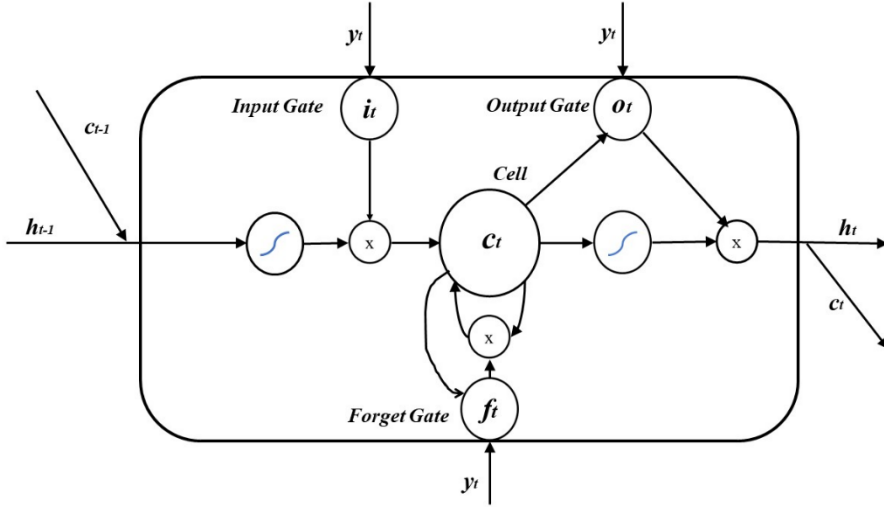


Fig. 2 The architecture of LSTM unit-neuron

As shown in the figure, the LSTM neuron provides a nonlinear mechanism for controlling information flow into and out of the LSTM cell. The forget gate determines the information that need to be discarded or forgotten from the previous cell states. The input gate determines what information will be allowed to enter into the neuron state. Finally, the output gate decides the information to be passed out of neuron state. Mathematically, the representation for the forward pass of an LSTM unit with a forget gate for $y_t : \{1, 2, \dots, n\} \rightarrow R^d$ (input vector to the LSTM unit; for (1), $d=1$), is as follows, [14]

$$f_t = \sigma_g (W_f y_t + U_f h_{t-1} + b_f) \quad (11)$$

$$i_t = \sigma_g (W_i y_t + U_i h_{t-1} + b_i) \quad (12)$$

$$o_t = \sigma_g (W_o y_t + U_o h_{t-1} + b_o) \quad (13)$$

$$c'_t = \sigma_c (W_c y_t + U_c h_{t-1} + b_c) \quad (14)$$

$$C_t = f_t \circ c_{t-1} + i_t \circ c'_t \quad (15)$$

$$h_t = o_t \circ \sigma_h (C_t) \quad (16)$$

The initial values are $c_0 = 0$ and $h_0 = 0$ and the operator \circ denotes the Hadamard product (element-wise product). Variables are: $f_t \in (0,1)^h$ - forget gate's activation vector; $i_t \in (0,1)^h$ - input/update gate's activation vector; $o_t \in (0,1)^h$ - output gate's activation vector; $h_t \in (-1,1)^h$ - hidden state vector or output vector of the LSTM unit; $c'_t \in (-1,1)^h$ - cell input activation vector; $c_t \in R^h$ - cell state vector; $W \in R^{h \times d}$, $U \in R^{h \times h}$ and $b \in R^h$ weight matrices and bias vector parameters which need to be learned during training where the superscripts, f , i and h refer to the number of forget, input features and number of hidden units, respectively. Activation functions $\sigma - \sigma_{g,c,h}$ are, respectively: sigmoid, hyperbolic, or, identic function. SGDM is a stochastic optimization method that adds the expression of the corresponding impulse to the known stochastic descent gradient in the parameter

space. This achieves a faster convergence of the local minimum. Also, in the case of a shallow local minimum, this moment may be sufficient for the gradient to eject the local solution, which is a great advantage over the standard method.

c) ELM

ELM [4], [18-23] was first introduced to improve the efficiency and speed of a single-hidden-layer feedforward network. The ELM algorithm, as contrasting to the conventional belief of ANN theory, linear theory, and control theory, does not require hidden nodes/neurons and is a training algorithm for the single hidden layer feedforward neural network (SLFN). Unlike standard ANN, that periodically assigns hidden nodes, ELM randomly assigns hidden nodes, constructs biases and input weights of hidden layers, and determines the output weights using least squares methods. This significantly justifies the low computational time of ELM. Different than gradient based methods, ELM assigns random values to the weights between input and hidden layer and the biases in the hidden layer, and these parameters are frozen during training. The nonlinear activation functions in hidden layer provide nonlinearity for the system. Then, it can be regarded as a linear system. The only parameter that network needs to learn is the weight between a hidden layer or the threshold of the hidden layer and output layer. Hence, ELM converges much faster than traditional algorithms because it learns without iteration. Random hidden nodes promise the universal approximation ability. Theoretical analysis showed that ELM is more likely to reach global optimal solution with random parameters than traditional networks with all the parameters to be trained [18-22]. Compared with the support vector machine (SVM) [13]. ELM tends to yield better classification performance with less optimization constrains. Due to its superior training speed and good generalization capability, ELM is widely applied in a variety of learning problems, such as classification, regression, clustering, and feature mapping, [4], [18-23].

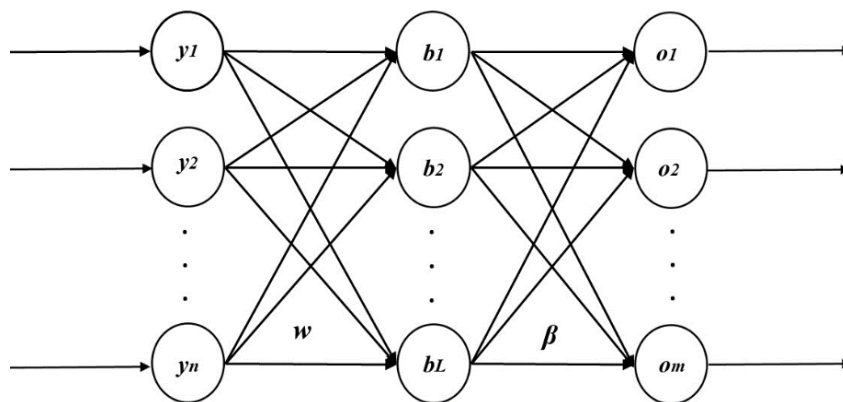


Fig. 3 Structure of SLFN.

The training problem for ELM is given in [22]. The schematic diagram of ELM is presented in Fig.3, [22]. A training set is $S = \{(\mathbf{y}_i, \mathbf{t}_i) \mid \mathbf{y}_i = (y_{i1}, y_{i2}, \dots, y_{in})^T \in R^n, \mathbf{t}_i = (t_{i1}, t_{i2}, \dots, t_{im})^T \in R^m\}$, where \mathbf{y}_i denotes the input value and \mathbf{t}_i represents the target,

where m is the number of output layer nodes. The output \mathbf{o}_j of an ELM with L hidden neurons, N - number of training samples, can be expressed as

$$\mathbf{o}_j = \sum_{i=1}^L \beta_i \sigma(\mathbf{w}_i \mathbf{y}_j + b_i), j = 1, \dots, N. \quad (17)$$

In ELM, activation functions σ are nonlinear ones to provide nonlinear mapping for the system. The set of vectors \mathbf{w}_i is the weight vector for the input layer in the i -th hidden node, b_i is the value of the bias in the i -th hidden node, β_i is the weight vector for the output layer in the i -th hidden node. The goal of training is to minimize the error between the target and the output of ELM. The most commonly used object function is mean squared error (MSE), defined as

$$MSE = E \left(\sum_{j=1}^N (\mathbf{y}_j - \mathbf{o}_j) \right) \quad (18)$$

where N is the number of training samples, and i and j are the indexes for the training sample and output layer node.

The basic training of ELM can be regarded as involving two steps: random initialization and linear parameter solution. Firstly, ELM uses random parameters \mathbf{w}_i and b_i in its hidden layer, and they are frozen during the whole training process. The input vector is mapped into a random feature space with random settings and nonlinear activation functions which is more efficient than those of trained parameters. In the second step, β_i can be obtained by Moore-Penrose inverse [22].

Besides MSE, for assessing the quality of prediction, RMSE (root mean square error)

$$RMSE = \sqrt{MSE} \quad (19)$$

and determination coefficient R^2

$$R^2 = \frac{E \left(\sum_{j=1}^N \mathbf{o}_j \mathbf{y}_j \right) - E \left(\sum_{j=1}^N \mathbf{o}_j \right) E \left(\sum_{j=1}^N \mathbf{y}_j \right)}{E \left(\sum_{j=1}^N \mathbf{o}_j \right) E \left(\sum_{j=1}^N \mathbf{y}_j \right)}. \quad (20)$$

are also used.

Other criteria for assessing the quality of time series models known in the literature are: Schwarz–Bayesian information criteria (SBC), sum of squares error (SSE), mean absolute percentage error (MAPE), Mean Average Error (MAE), and final prediction error (FPE), [1-6], [28-30].

Basic ELM training includes two steps: random initialization and solving a linear parameter problem. First, ELM uses the generated random weights and bias parameters \mathbf{w}_i and b_i in its hidden layer, whose values do not change throughout the training process. The input vector is mapped to a random state space determined by random properties and nonlinear activation functions, which turns out to be a more efficient way than that with trained parameters. In the second step, β_i is calculated via the Moore-Penrose inverse of \mathbf{H} , acting on \mathbf{t}_j [22]. They are further used to calculate the vector of output values \mathbf{o}_j

Possible areas of application of specific ELM algorithms are: recognition of objects in images, various classification problems, analysis of large amounts of data, hybrid online

learning, Self-Organizing Extreme Learning Machine (SOELM), processing unbalanced data, extremely fast ML, etc. However, ELM is faster than many ANN methods. With simple implementation, ELM performance is good in terms of accuracy as well.

3. NUMERICAL RESULTS

The most illustrative numerical results related to the application of the SARIMA model and ANN models in forecasting the volume of packages in the internal postal traffic of Serbia are presented here. We considered the monthly data for the period 2014-2020.

The logarithm of the total volume of internal parcel postal traffic in the Republic of Serbia for the entire considered period is shown in Fig. 4. This procedure of logarithmic scaling reduces the scope of the data set and thus simplifies the calculation.

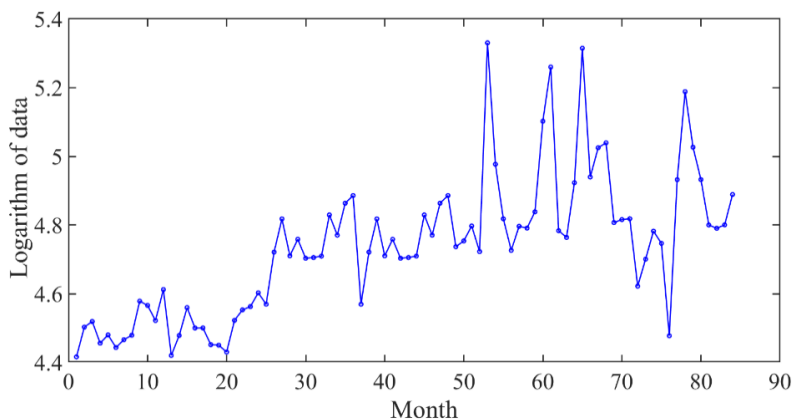


Fig. 4 Logarithm of the volume of internal parcel postal traffic of Serbia - original data, 84 monthly observations - period from January 2014 to December 2020.

XLSTAT software environment was used to find the best (S)ARIMA basic model properties and parameters, on the basis of which the analysis was continued in the MATLAB environment. MATLAB was also used for forecasting time series data using the LSTM network and ELM.

The best values of (S)ARIMA parameters (p, P, d, D, q, Q, s) can be determined in XLSTAT. For thus obtained values the model evolves by the aid of the process presented in Fig. 1. The procedure for obtaining the numerical values of parameters, criteria and graphic solutions is fast, and the work on establishing the group of statistical models is efficient. Some parameters and criteria of models are described in [5], [26-29] and supplied in this paper. The convergence values (10^{-5}) and maximal number of iterations (5000) were specifically selected, $s=0, 12$, and confidence interval is always 95%. In an XLSTAT environment the maximum values for d, D are set to be 1, and for p, P, q, Q are 4. The best obtained value for AICC is $-77,8888$ within the work on several hundreds of cases of various parameters and model parameters for this model are selected. The convergence towards this solution has been made in 40 iterations over the measurement subset for these 72 observations.

All the optimal affirmative statistics is shown in the Table 1. The model parameters, without $s=0$, (S)ARIMA (Eq.(2)) are provided in the Tables 2 and 3. The value of the trend component is provided in the Table 2. Based on hundreds of analyzed (S) ARIMA approaches in the XLSTAT environment of a given time series, in addition to noticing small values of basic parameters, it is recognized that the best model is not seasonal. The values of the parameters AR(1), MA(1) and MA(2) are presented in the Table 3. The value of RMSE=0.131536.

Table 1 Goodnes of fit statistics

Observations	72
DF	68
SSE	1.24572
MSE	0.017302
RMSE	0.131536
WN Variance	0.017302
MAPE(Diff)	1.779189
MAPE	1.779189
-2Log(Like.)	-86.4858
FPE	0.017789
AIC	-78.4858
AICC	-77.8888
SBC	-69.3791
Iterations	40

Table 2 SARIMA trend component

Parameter	Value	Hessian standard error
Trend component	4.680	0.127

Table 3 SARIMA model parameters

Parameter	Value	Hessian standard error
AR(1)	0.975	0.030
MA(1)	-0.493	0.130
MA(2)	-0.215	0.120

The value of the basic probability parameter is $-2\text{Log}(\text{Likelihood}) = -86.4858$. The SBC parameter has a value of -69.3791 , which is, in theory, correct, that is, the smallest. This value serves as the criterion for selecting the model within the final set of models and is related to the Akaike information criterion.

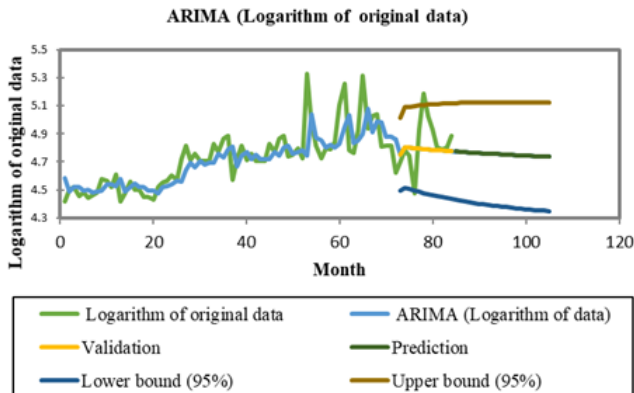


Fig. 5 Results of XLSTAT simulation for the logarithm of internal parcel postal traffic of Serbia, 84 monthly observations - period from January 2014 to December 2020.

The total results of the XLSTAT simulation are summarized in Fig. 5. In addition to the logarithms of the original data, their ARIMA values, validation, and prediction data, as well as the lower and upper 95% bounds of the prediction are given. Simulation results for 84 elements are given, including validation (last 12 members of the time series) and prediction (21 new members, from month 85 to 105). Confidence interval bounds (95%) are set for validation and prediction. For last 21 members of the time series, the values of characteristic validation parameter values are $RMSE=0.1804$ and $R^2 = 0.0673$. The graph of the dependence of residual values on the number of months (84 in total) is shown in Fig. 6. The maximum of residuals is for month 54.

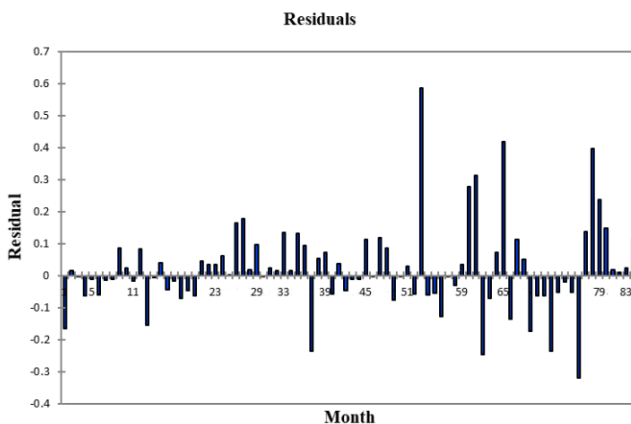


Fig. 6 XLSTAT residual graph for the logarithm of the volume of internal parcel postal traffic of Serbia.

XLSTAT descriptive analysis – determining the values of p and q (ACF and PACF) for a given time series is shown in Fig. 7 and Fig. 8. The obtained values are PACF – $p = 1$, ACF – $q = 1$ (cutoff after lag =1, according to the previously stated procedure after Eqs. (7) and (8)).

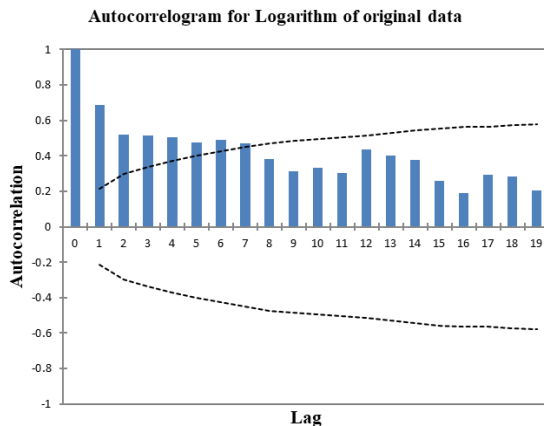


Fig. 7 XLSTAT ACF graph for the logarithm of the volume of internal parcel postal traffic of Serbia.

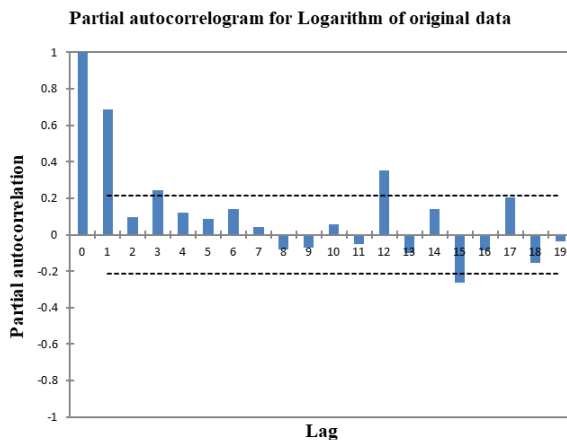


Fig. 8 XLSTAT PACF graph for the logarithm of the volume of internal parcel postal traffic of Serbia.

XLSTAT descriptive analysis (ACF and PACF) for residuals is shown in Fig. 9 and Fig. 10. By definition, PACF provides a partial correlation of a stationary time series with its own lagged values. Here, the results are $P=0$, $Q=0$ (cutoff after lag=0, due to small autocorrelations, according to the previously stated procedure). According to the results presented in Fig. 5 – Fig. 10, integrated process ARIMA (1,0,1) (0,0,0)₀ is proposed.

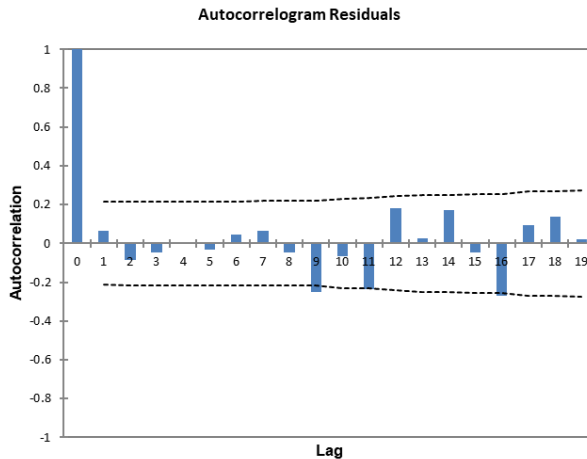


Fig. 9 XLSTAT ACF graph for residuals of the logarithm of the volume of internal parcel postal traffic of Serbia.

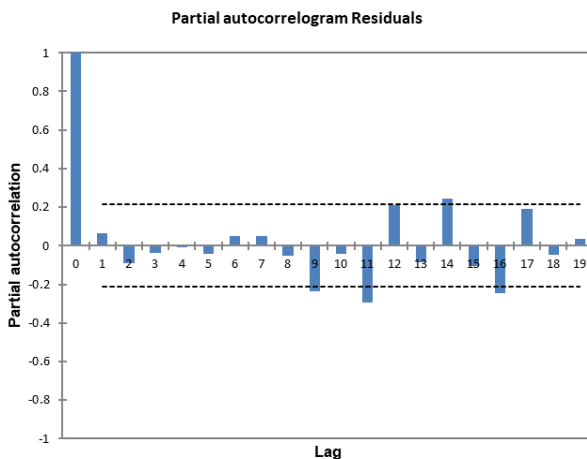


Fig. 10 XLSTAT PACF graph for residuals of the logarithm of the volume of internal parcel postal traffic of Serbia.

Prediction of data of the same time series was also done using the LSTM network in the MATLAB Deep Learning Toolbox.

For forecasting the last 21 time series values, LSTM is trained by sequence-to-sequence regression, using previous 63 members, and the training sequence responses are compared to actual time series values, shifted one step forward. LSTM network contains a sequence input layer, an LSTM layer having 200 hidden units, a fully connected layer, and a regression output layer. For the LSTM regression network training, an SGDM optimizer is used, and it was trained for 400 epochs, with the use of the state of forecasting and improvement. Sub-commands used, apart from the standard ones: *Momentum* (moment

value from interval (0, 1) which corrects the current value of stochastic gradient) and *L2Regularization* (multiplier of network layers' parameters, introduced for their regularization, field of value is up to 0.1). The values of characteristic parameters are $RMSE = 0.24585$ and $R^2 = 0.011866$. The comparison of the LSTM model forecast the data of the original time series, as well as their difference, is shown in Fig. 11.

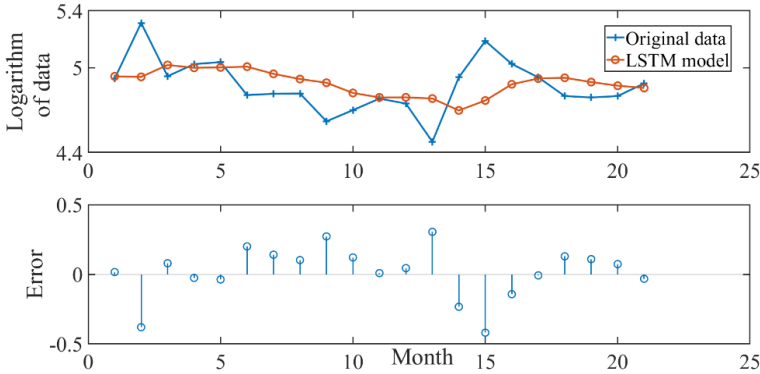


Fig. 11 LSTM forecast and corresponding errors - the differences between validation and observed datasets, values related to the logarithm of the volume of internal parcel postal traffic of Serbia.

ELM programs within MATLAB were used for the improvement of ARIMA and LSTM forecast data. As for both, the first 63 members of the original sequence are used for the training, and the remaining 21 data (test group) are from the original ARIMA and LSTM series. The initial values of the weight vector, \mathbf{w} , and bias, \mathbf{b} , (equation (17)) are generated randomly. Various transfer functions are tested, such as sigmoid, sinusoidal, and so-called unit hardlim function and the first one proved to be the best. In order to reduce the value of RMSE and increase the value of R^2 , in the simplest case, the procedure was repeated several times, with the appropriate program conditions. It has been observed that the optimal number of iterations is 200,000 per 1 million such iterations for different initial machine-generated random conditions. Regarding the improvement of the ARIMA forecasting, the following values $RMSE=0.12985$ and $R^2=0.59921$ are obtained. The ELM method was applied to the results of 63 LSTM training data. The obtained results (21 of them) were compared with the original data and the following prediction quality is achieved: $RMSE = 0.14561$ and $R^2 = 0.59905$.

In order to reach 200000 iterations in ELM, the simulations of up to 10^6 iterations for each problem were made, with the increases up to 100000. There was no improvement in RMSE and R^2 values above 200000, which means that in this way, the relatively fast convergence of these parameters value cannot be implemented.

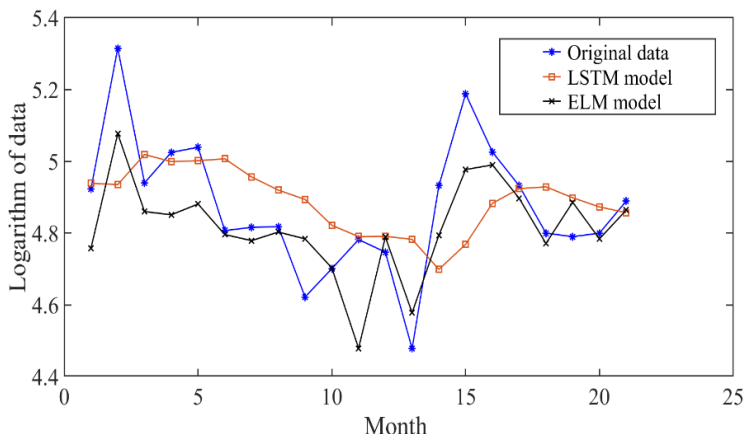


Fig. 12 Comparison of the test set results (21 data) of LSTM method and ELM method with the original data

The comparison of the results obtained by applying the two proposed methods with the original data is shown in Fig.12. While LSTM proved to be better for tracking the original data at the ends, ELM better represented the initial group, as a whole. The ELM method has the best performances in terms of RMSE and R² values compared to ARIMA and LSTM. The practical division into 63 training elements and 21 test group elements within all possible modeling was selected after studying the partition containing 72 training elements and 12 test group elements. It was estimated that the possible improvements of all methods in the two cases regarding RMSE according to the number of test data are approximately 10⁻⁵.

5. CONCLUSION

The combined data analysis techniques based on the ARIMA statistical model, as well as LSTM and ELM neural network models are presented in the paper. The analysis was performed on a series of consecutive monthly data representing the volume of packages in the internal postal traffic of Serbia for the period 2014-2020.

The easy-to-use XLSTAT EXCEL software environment was first used to find the basic parameters of the (S)ARIMA model. The results were supplemented by the analysis of source and residual ACF and PACF time series data. A similar way of processing data, of the same time series, using the LSTM network trained in the MATLAB Deep Learning Toolbox was also considered. The modeling results obtained by the LSTM method were compared with the original data. The results of the ARIMA and LSTM methods were then used to improve the predicted ELM values. The ELM method was applied to the results of the ARIMA and LSTM methods in order to improve and obtain a more accurate prognosis. The obtained results of ELM methods, in both cases (for the LSTM model and for the ARIMA model), were compared with the original data. The obtained RMSE value for the ELM model was found to be about 28% lower than the corresponding one for the ARIMA model.

This way of combining and comparing the above forecasting methods is a significant novelty in relation to the application of previous individual techniques, both in terms of quality of results and methodology.

Acknowledgement: *This work was supported by the Ministry of Education, Science and Technological Development of Republic of Serbia (Grant No. 451-03-9/2021-14/200102).*

REFERENCES

- [1] Taeho Jo, *Machine Learning Foundations: Supervised, Unsupervised, and Advanced Learning*. Springer Nature Switzerland AG, 2021.
- [2] Manjusha Pandey; Siddharth Swarup Rautaray, *Machine Learning: Theoretical Foundations and Practical Applications*. Springer Nature Singapore Pte Ltd. 2021.
- [3] <https://ai.stanford.edu/people/nilsson/mlbook.html>
- [4] arXiv:2012.03854v2 [stat.AP] 3 Jun 2021. Available: <https://arxiv.org/pdf/2012.03854v1.pdf>
- [5] G.E. Box, G.M. Jenkins, G.C. Reinsel, G. M. Ljung, *Time Series Analysis, Forecasting and Control*. New Jersey, John Wiley and Sons, 2016.
- [6] R. J. Hyndman, G. Athanasopoulos, *Forecasting: principles and practice*. 3rd edition, OTexts: Melbourne, Australia. OTexts.com/fpp3. Accessed on 26 September 2021.
- [7] D. C. S. Bisht (eds.), M. Ram (eds.), *Recent Advances in Time Series Forecasting*. Boca Raton, CRC Press, 2021.
- [8] A. Ticherahine, A. Boudhaouia, P. Wira and A. Makhlof, "Time series forecasting of hourly water consumption with combinations of deterministic and learning models in the context of a tertiary building," Int.Conf. on Decision Aid Sciences and Application, 2020.
- [9] H. Yu, L. Jingming, R. Sumei, Z. Shuping, "Hybrid Model for Financial Time Series Forecasting – Integration of EWT, ARIMA with The Improved ABC Optimized ELM," IEEE Access, 1–1. doi:10.1109/access.2020.2987547.
- [10] B. Predić, N. Radosavljević, A. Stojić, "Time Series Analysis: Forecasting Sales Periods in Wholesale Systems," Facta universitatis, Series: Automatic Control and Robotics, vol. 18, no 3, pp. 177–188, 2019.
- [11] M. Paluszek, S. Thomas, *MATLAB Machine Learning Recipes: A Problem-Solution Approach*. Second Edition, New Jersey, Apress, 2019.
- [12] M. Paluszek, S. Thomas, *Practical MATLAB Deep Learning: A Project-Based Approach*. New Jersey, Apress, 2020.
- [13] S. Hochreiter, J. Schmidhuber, "Long short-term memory", *Neural Computation*. 9 (8): 1735–1780, 1997.
- [14] arXiv:1303.5778v1 [cs.NE] 22 Mar 2013.
- [15] <https://www.mathworks.com/help/deeplearning/ref/sgdmupdate.html> .
- [16] A. Voelker, I. Kajić, C. Eliasmith, "Legendre Memory Units: Continuous-Time Representation in Recurrent Neural Networks," 33rd Conference on Neural Information Processing Systems NeurIPS Vancouver, Canada, 2019.
- [17] P. Poonia, V. K. Jain, "Short-Term Traffic Flow Prediction: Using LSTM", IEEE, International Conference on Emerging Trends in Communication, Control and Computing, 2020.
- [18] Guang-Bin Huang, Qin-Yu Zhu, Chee-Kheong Siew, "Extreme learning machine: theory and applications," *Neurocomputing*. 70 (1): 489–501, 2006.
- [19] Guang-Bin Huang, Qin-Yu Zhu, K. Z. Mao, Chee-Kheong Siew, P. Saratchandran and N. Sundararajan, "Can threshold networks be trained directly?" in *IEEE Transactions on Circuits and Systems II: Express Briefs*, vol. 53, no. 3, pp. 187-191, March 2006, doi: 10.1109/TCSIL.2005.857540.
- [20] G. -B. Huang, H. Zhou, X. Ding and R. Zhang, "Extreme Learning Machine for Regression and Multiclass Classification," in *IEEE Transactions on Systems, Man, and Cybernetics, Part B (Cybernetics)*, vol. 42, no. 2, pp. 513-529, April 2012, doi: 10.1109/TSMCB.2011.2168604.
- [21] Guang-Bin Huang, "What are Extreme Learning Machines? Filling the Gap Between Frank Rosenblatt's Dream and John von Neumann's Puzzle," *Cognitive Computation*, volume 7, issue 3 2015.
- [22] J. Wang, S. Lu, Shui-Hua Wang, Yu-Dong Zhang, "A review on extreme learning machine," *Multimed Tools Appl*, 2021. [Online]. Available: <https://doi.org/10.1007/s11042-021-11007-7> .
- [23] <https://elmorign.wixsite.com/originofelm> .
- [24] <https://www.programmingsought.com/article/231014377/>

- [25] <https://www.xlstat.com/en/>.
- [26] <https://www.mathworks.com/help/econ/estimate-multiplicative-arimamodel-using-econometric-modeler.html> .
- [27] N. Knežević, N. Glišović, M. Milenković, N. Bojović, “Neural Networks Based on Metaheuristics for Forecasting the Revenue of Postal Services,” (in Serbian), PosTel 2018, pp.33-42, Belgrade, Serbia, 2018.
- [28] I. D. Rogan, O.R. Pronić-Rančić, “Forecasting the volume of postal services using Savitzky-Golay filter modification,” Sozopol, Bulgaria, 56th International Scientific Conference on Information, Communication and Energy Systems and Technologies (ICEST), 2021. DOI: 10.1109/ICEST52640.2021.9483459.
- [29] I. D. Rogan, O.R. Pronić-Rančić, “SARIMA and ANN Approaches in Forecasting the Volume of Postal Services,” Niš, 15th International Conference on Advanced Technologies, Systems and Services in Telecommunications, TELSIKS, 2021.
- [30] C. M. Hurvich, Chih-Ling Tsai, “Regression and time series model selection in small samples”, *Biometrika*, vol. 76, no. 2, pp. 297-307, 1989.
- [31] <https://www.posta.rs/eng/stanovnistvo/usluga.aspx?usluga=postal-services/parcel-services-serbia/sending-parcels-within-serbia>

THE WINDER DANCER POSITION CONTROL MODEL USING DIFFERENT PID CONTROL STRUCTURES AND MICROLOGIX PLC

UDC (681.518.52+621)

**Saša S. Nikolić¹, Igor Kocić¹, Dragan Antić¹, Darko Mitić¹,
Nikola Danković¹, Aleksandra Milovanović¹, Petar Đekić²**

¹University of Niš, Faculty of Electronic Engineering, Department of Control Systems,
Republic of Serbia

²The Academy of Applied Technical and Preschool Studies-Niš, Republic of Serbia

Abstract. *In the cable industry, improper regulation of the winding speed of the conductor cable, i.e. the position of the tensioner (dancer) leads to improper stretching of the conductor, which significantly affects the characteristics of the final product. Winding speed control is directly related to tensioning which is an additional problem. This paper presents a system for control a cable winding device using a linear PID controller with and without control signal limitation. The system parameters were determined using integral time-weighted absolute error (ITAE) criteria and realized using a conventional PLC controller.*

Key words: *Winder dancer, PID controller, PLC controller, ITAE criteria*

1. INTRODUCTION

In the cable industry, the improper regulation of the winder speed or the dancer position leads to the stretching of the conductors, which significantly affects the final product's characteristics. The winder speed control is directly related to the tightening, which becomes an additional issue. The complexity of the regulation is reflected in nonlinearities that exist due to the influence of friction, stretching, sliding, variation of the moment of inertia of a drum during work, etc. Due to importance in this type of industry, such regulation problems attract the attention of many researchers.

Received April 09, 2022 / Accepted May 18, 2022

Corresponding author: Saša S. Nikolić

University of Niš, Faculty of Electronic Engineering, Department of Control Systems, Aleksandra Medvedeva
14, 18000 Niš, Republic of Serbia

E-mail: sasa.s.nikolic@elfak.ni.ac.rs

For the regulation of the winder speed in earlier systems, the PI regulation [1] was used mostly. Due to significant variations of parameters in the system dynamics which is reflected in the change in diameter of the winder's drum due to the accumulation of windings, the regulation using PI regulator turned out as inadequate. As an improvement, K. Reid, K. Shin and K. Lin [2, 3] proposed a method of changing amplifications in dancer's working range.

Practically all PID controllers in the industry today are based on some of PLC controller's regulation or its modified variants [4]. PLC controllers offer commands for the realization of linear PID control in the form of a monitoring error with fixed amplifications [4, 5]. As a result, it often reduces the system performance because the compromise between the exceeding value and the response speed is being made. For improving the performances of the system significantly, the non-linear controller should be used, which inevitably makes the system more complex.

2. DANCER AND WINDING SYSTEM MODEL

The winding device [6] consists of a dancer, a winder drive engine and a winder with drums (Fig. 1). The dancer is also a provider of the current position. The moving roll is connected to a position giver by the pneumatic cylinder. The signal from the position giver is brought to the regulator which generates the control signal. Basically, the simplest type of regulation is reflected in the following: The dancer position signal is sent as a reference to the regulator which accelerates or decelerates the winder drive engine depending on the position of the dancer itself. The dancer position converts to an analog signal. As a position giver, the analog output sensor, or some modern angle position sensor is used.

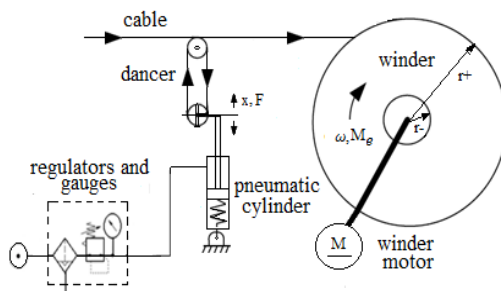


Fig. 1 Principal scheme of winder speed and line-up device step regulation

The DC engine is harnessed via a moment transmission system with a drum. The cause of the position change of the dancer is the difference between the speeds of the winder and the part of the line that delivers conductor to it.

The recording of the dancer's bouncing response is performed using KepwareEx server [7] that is set to read and write the values from the register of the N7 PLC controller, which are the signals of the dancer's position, the position set point and the control signal, respectively, into suitable fields of the base. The jumping change of the speed is achieved using the DC regulator for the winder drive engine that is started

manually with the acceleration ramp of 0.1s. For the recording of the bouncing response, the dancer's starting position is set to $x=0.6m$. The value of the incentive signal changes for each recording. The dancer's working range is from 0 to 1.2m. Recording is performed for three different control signal values. In Fig. 2 a real dancer and model are shown.

Based on the recorded feature, the dancer model is determined. The dancer is basically NSMD [6] (*Non-linear Spring Mass Damping*) system consisting of the upper fixed roll and a lower moving roll coupled with a pneumatic cylinder (Fig. 2). The dancer model is presented with a mass m , a damping coefficient B with the function of spring elasticity: $f(x) = k_1x_1 + k_2x_1^3$. The position of the dancer is converted to the value corresponding to the position of the dancer using the analog module of the PLC controller. Scaling commands are used to convert to engineering units. The value of 8196 corresponds to the working position (0.6m) and the value of 16000 corresponds to the lower position of the dancer (1.2m).

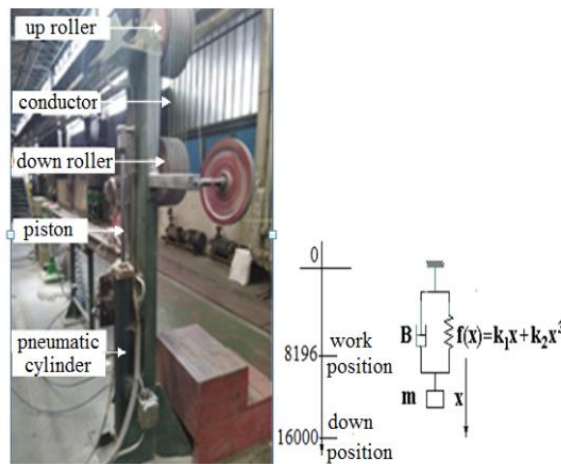


Fig. 2 A real dancer and the dancer model with a pneumatic cylinder with a spring

The parameters of the motor come from the nameplate of the engine, by the measurement of the characteristic values of the engine, doing the idling experiment and the experimentation for the determination of the moment of inertia and viscous friction coefficient.

The dancer model is given as follows:

$$\frac{d^2x}{dt^2} + f\left(x, \frac{dx}{dt}, B, k_1, k_2, r\right) = F \tag{1}$$

$$r \in (r^-, r^+).$$

The DC motor with the rotor current regulation model is given by:

$$u_a = R_a i_a + L_a \frac{di_a}{dt} + k_e \omega. \tag{2}$$

By arranging previous equations, the following relations are obtained:

$$\frac{d^2x}{dt^2} = \frac{k_m}{mr} i_a - \frac{B}{m} \frac{dx}{dt} - \frac{f(x)}{m} x, \tag{3}$$

$$i_a = \frac{1}{L_a} u - \frac{k_e}{L_a r} \frac{dx}{dt} - \frac{R_a}{L_a} i_a. \tag{4}$$

By introducing: $x_1 = x$, $x_2 = \dot{x}$, $x_3 = i_a$, and by arranging, we get a system model in state space:

$$\begin{aligned} \dot{x}_1 &= x_2 \\ \dot{x}_2 &= -\frac{k_1 x_1 + k_2 x_1^3}{m} - \frac{B}{m} x_2 + \frac{k_m}{mr} x_3 \\ \dot{x}_3 &= -\frac{k_e}{L_a r} x_2 - \frac{R_a}{L_a} x_3. \end{aligned} \tag{5}$$

i.e., $\dot{x} = F(x) + g(x)u$, in matrix form:

$$\begin{bmatrix} \dot{x}_1 \\ \dot{x}_2 \\ \dot{x}_3 \end{bmatrix} = \begin{bmatrix} x_2 \\ -\frac{k_1 x_1 + k_2 x_1^3}{m} - \frac{B}{m} x_2 + \frac{k_m}{mr} x_3 \\ -\frac{k_e}{L_a r} x_2 - \frac{R_a}{L_a} x_3 \end{bmatrix} + \begin{bmatrix} 0 \\ 0 \\ \frac{1}{L_a} \end{bmatrix} u \tag{6}$$

Based on Eq. (6), the winder system is drawn. In Fig. 3, the Simulink winder system is shown, with the value of the diameter (r) as a constant value.

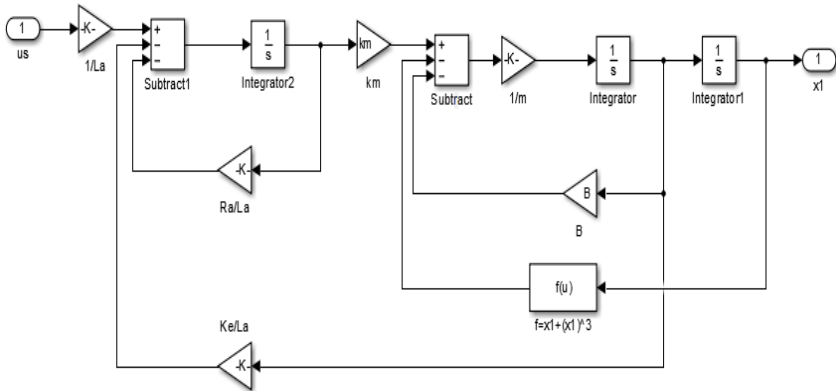


Fig. 3 Dancer and drive engine model

3. DESCRIPTION OF THE METHOD FOR ADJUSTING THE CONTROLLER PARAMETERS

Setting the controller parameters is performed using ITAE criteria. The optimal values k_p , k_i , and k_d of the PID controller are determined [7]-[10] which minimize the goal function:

$$J = \int_0^{\infty} |e(t)| dt . \tag{7}$$

The integral (7) is calculated using Simpson’s 1/3 rule (8) and represents the approximate solution of the integral, and in accordance with it, the program is written in Matlab. The program in Matlab as variables uses controller’s parameters [11, 12]:

$$\int_a^b f(x)dx \approx \frac{h}{3} (f_0 + 4 \sum_{i=1}^m f_{2i-1} + 2 \sum_{i=1}^{m-1} f_{2i} + f_{2m})$$

$$h = \frac{b-a}{m} . \tag{8}$$

where represents a and b are the endpoints of integrations, interval of integration $[a, b]$ split up into m sub-intervals, m is an even number, $h=(b-a)/m$ is the step length, m is the midpoint of integration interval $[a, b]$.

The adjustment of the linear PID regulator of the winder system is performed using Matlab and Simulink. The setting procedure consists of the following steps:

1. For a closed loop feedback system with the known transmission function, the critical gain $(k_p)_{kr}$ and cross phase frequency $(\omega\pi)_{kr}$ are determined by using a suitably written program in Matlab,
2. For the initial values of the regulator parameters, the values for k_p , k_i , and k_d are determined by the Ziegler-Nichols rule for a closed loop system [8],
3. The values of parameters from the point 2 k_p , k_i , and k_d are used as the initial values for solving the integral (8),
4. In Simulink, the model of the process with the appropriate regulator is drawn,
5. Using the suitably written Matlab script for the integral solution (7), the toolbox optimization and Simulink system model, the optimal parameter values of the controller k_p , k_i , and k_d are determined by the criterion (8).

4. REALIZATION OF THE CONTROL SYSTEM

Control was realized using control scheme with PID regulator (9), Fig. 4. and Fig. 11 with their modifications in terms of the control signal limit [13]. In Figs. 5-10, and Figs. 12-

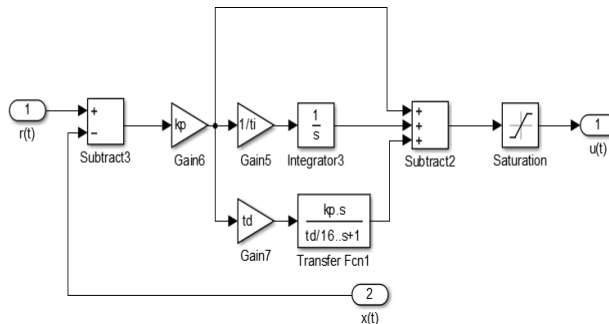


Fig. 4 Block scheme with PID control

17 the response and control signals are shown for all control scheme and their modifications, respectively.

PID regulator per error signal, with a limited output and a positively limited output is described with Eqs. (9)-(11):

$$u = u_s = k_p e + k_i \int e dt + k_d \frac{de}{dt}. \quad (9)$$

$$u = \begin{cases} +u_{\text{smax}}, & u > u_{\text{smax}} \\ k_p e + k_i \int e dt + k_d \frac{de}{dt}, & -u_{\text{smax}} \leq u \leq +u_{\text{smax}} \\ -u_{\text{smax}}, & u < -u_{\text{smax}} \end{cases} \quad (10)$$

$$u = \begin{cases} +u_{\text{smax}}, & u > u_{\text{smax}} \\ k_p e + k_i \int e dt + k_d \frac{de}{dt}, & 0 \leq u \leq +u_{\text{smax}} \\ 0, & u < 0 \end{cases} \quad (11)$$

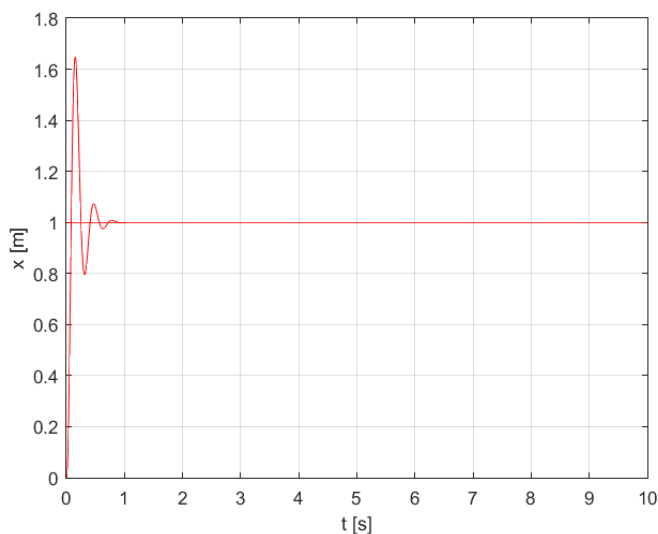


Fig. 5 Current dancer position characteristic for PID regulation per error signal according to (9)

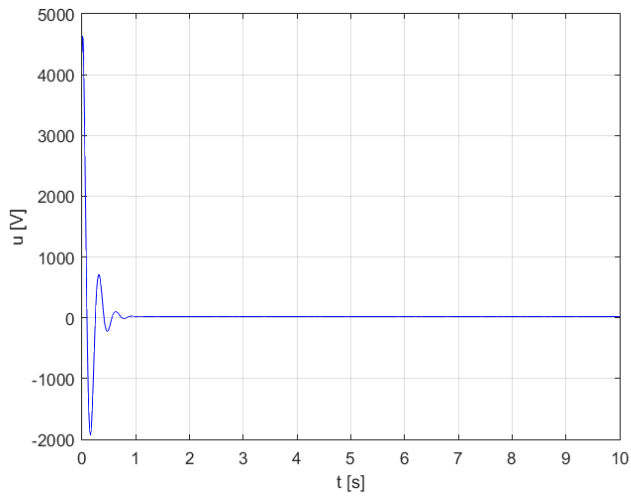


Fig. 6 Control signal characteristic for PID regulation per error signal according to (9)

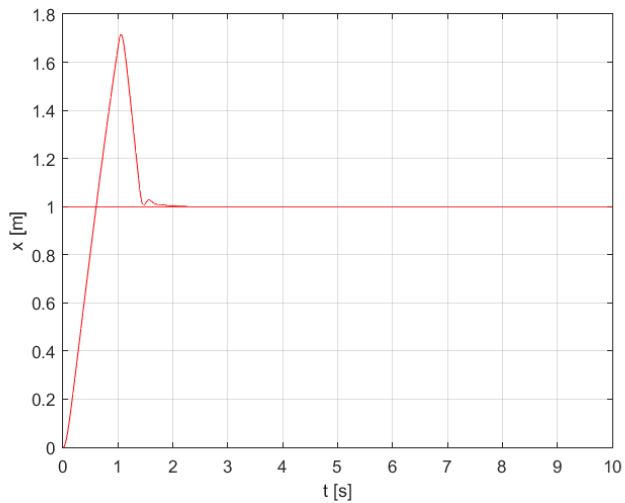


Fig. 7 Current dancer position characteristic for PID regulation per error signal with the control signal limitation on both sides (-m, +m) according to (10)

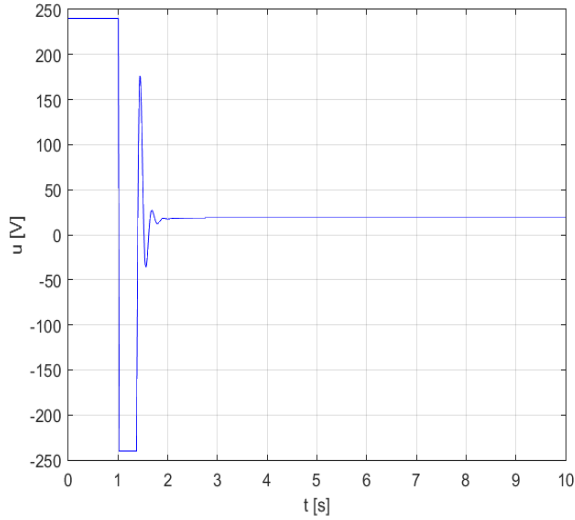


Fig. 8 Control signal characteristic for PID regulation per error signal with the control signal limitation on both sides (-m, +m) according to (10)

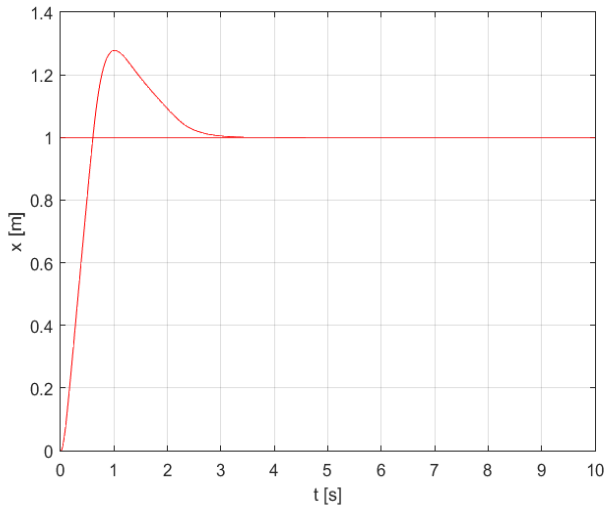


Fig. 9 Current dancer position characteristic for PID regulation per error signal with the control signal limitation on both sides (0, +m) according to (11)

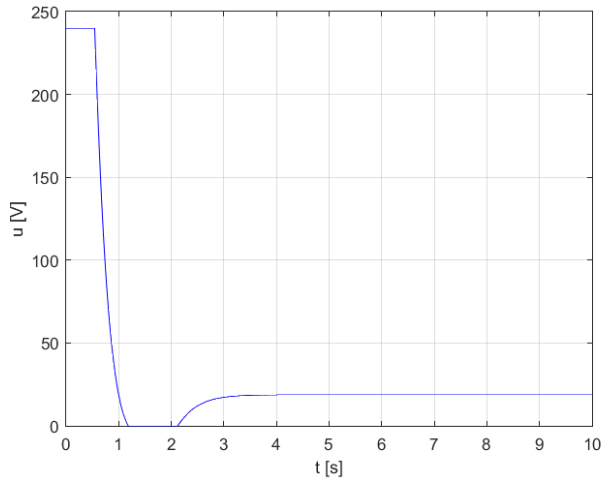


Fig. 10 Control signal characteristic for PID regulation per error signal with the control signal limitation on both sides (0, +m) according to (11)

PID with differential effect per the controlled variable, with a limited output and a positively limited output of Eqs. (12)-(14):

$$u = u_{s1} = k_p e + k_i \int edt + k_d \frac{dx}{dt} \tag{12}$$

$$u = \begin{cases} +u_{s1max}, & u > u_{s1max} \\ k_p e + k_i \int edt + k_d \frac{dx}{dt}, & -u_{s1max} \leq u \leq +u_{s1max} \\ -u_{s1max}, & u < -u_{s1max} \end{cases} \tag{13}$$

$$u = \begin{cases} +u_{s1max}, & u > u_{s1max} \\ k_p e + k_i \int edt + k_d \frac{dx}{dt}, & 0 \leq u \leq +u_{s1max} \\ 0, & u < 0 \end{cases} \tag{14}$$

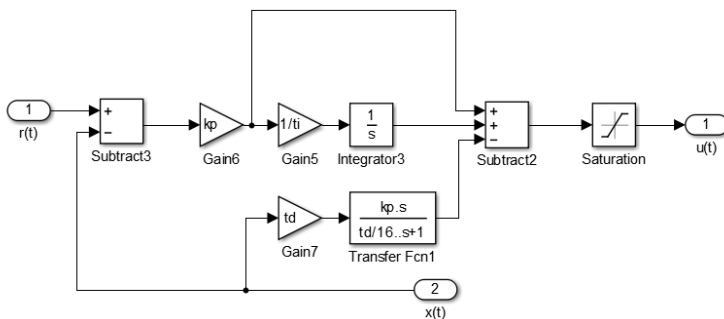


Fig. 11 PID with differential effect per position

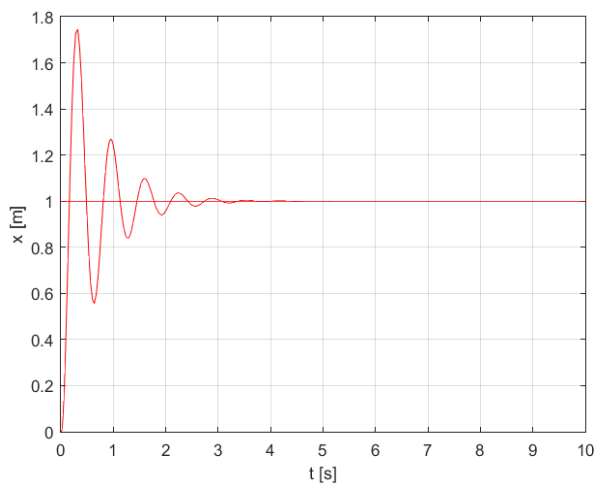


Fig. 12 Current dancer position characteristic for PID regulation with differential effect per position according to (12)

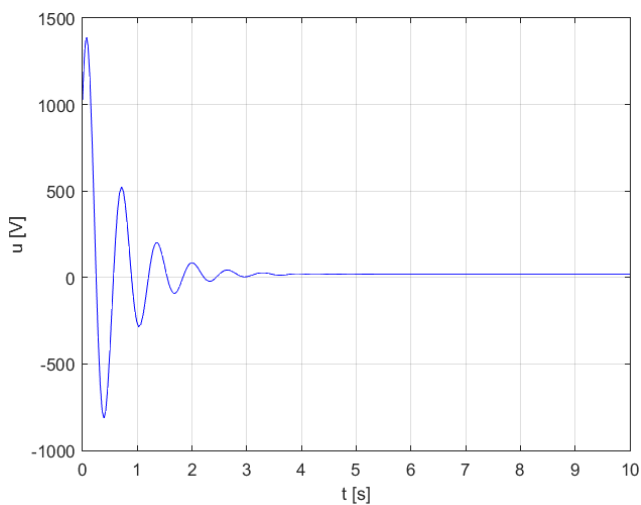


Fig. 13 Control signal characteristic for PID regulation with differential effect per position according to (12)

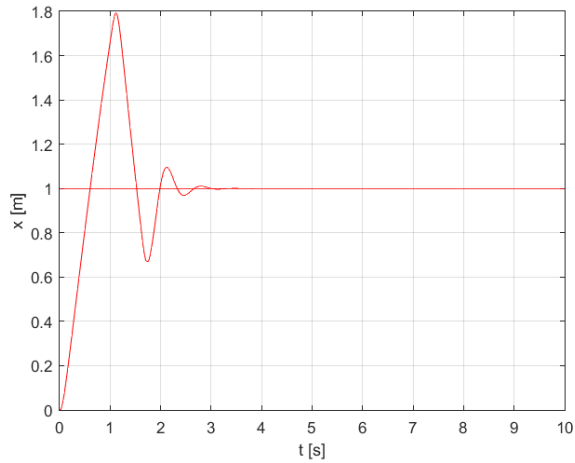


Fig. 14 Current dancer position characteristic for PID regulation with differential effect per position with the control signal limitation on both sides (-m, +m) according to (13)

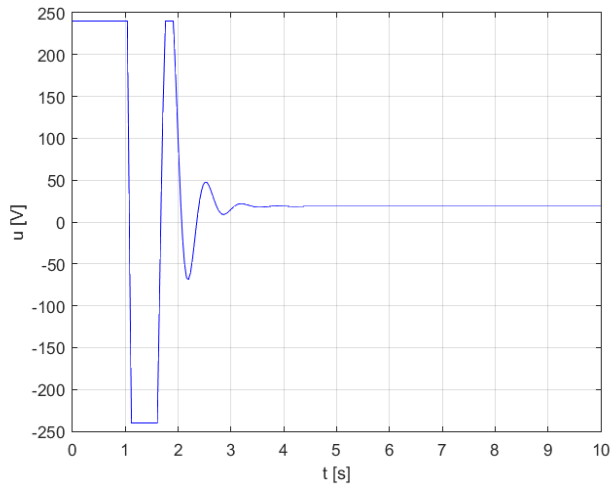


Fig. 15 Control signal characteristic for PID regulation with differential effect per position with the control signal limitation on both sides (-m, +m) according to (13)

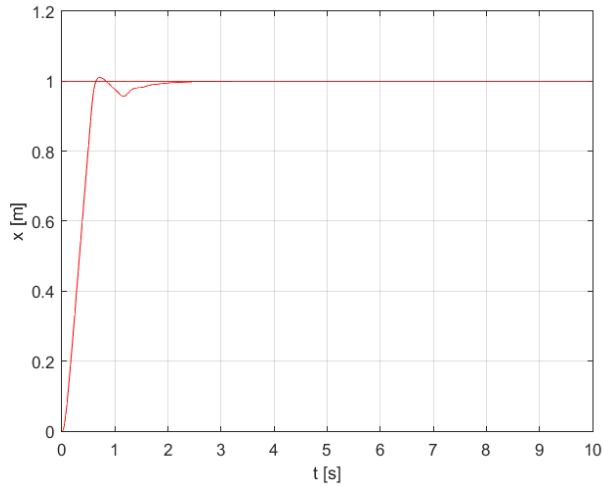


Fig. 16 Current dancer position characteristic for PID regulation with the differential effect per position with control signal limitation on both sides (0, +m) according to (14)

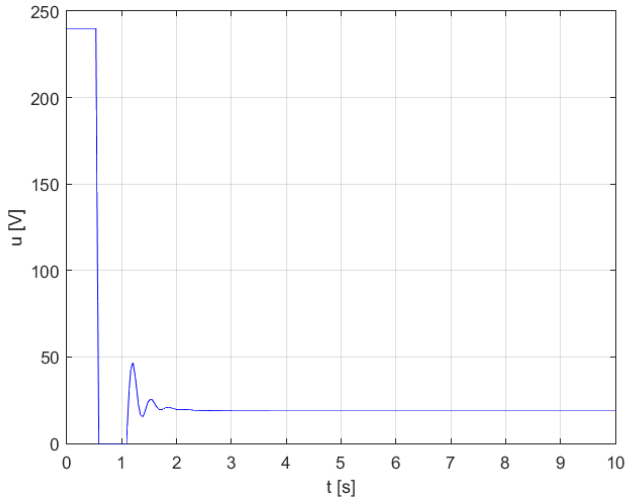


Fig. 17 Control signal characteristic for PID regulation with differential effect per position with control signal limitation on both sides (0, +m) according to (14)

5. DESCRIPTION OF HARDWARE AND SOFTWARE SOLUTIONS

To manage the process of winding the conductors on coils and drums uses, as a regulator, PLC Micrologix 1400 with SimoreG DC Master controller type 6RA7025 [5] for the drive of the engine [14]-[16]. The current dancer position is turned into a voltage signal by a 10 K Ω

potentiometer. The control signal from PID command of the PLC controller is sent to the analog input of the DC engine regulator, which regulates the speed of the drum on the winder and thus the position of the dancer.

The PID controller was realized using the Micrologix 1400 PLC's PID command with the following equation [14]:

$$u(t) = k_p \left[e(t) + \frac{1}{T_i} \int_0^t e(\tau) d\tau + T_d \frac{dc(t)}{dt} \right] + bias, \quad (18)$$

where: $u(t)$ - control signal, $e(t)$ - error signal, $c(t)$ - size management, k_p - proportional coefficient, T_i - integral time constant, T_d - differential time constant, $bias$ - value to compensate the impact of interference on the controlled variable.

The transfer function of the differential action of Eq. (18) was realized using a low-pass filter whose transfer function is given by equation:

$$G_d(s) = \frac{sT_d}{1 + s \frac{T_d}{N}}. \quad (19)$$

Parameter N defines the measure of the influence of the low-pass differential action filter. The value of parameter N of the Micrologix series of PLC controllers is set to $N = 16$. The manufacturer of the PLC controller does not provide any other data regarding the value for N and the methods for discretization of the PID control law (18) [11].

The PID is set to operate on an error signal (bit DA = 1). The Fig. 19 shows the PID command of the PLC controller with differential effect per position with the control signal limitation in the range of 0-10V which is suitable for the voltage of the engine's armature of 0-240V.

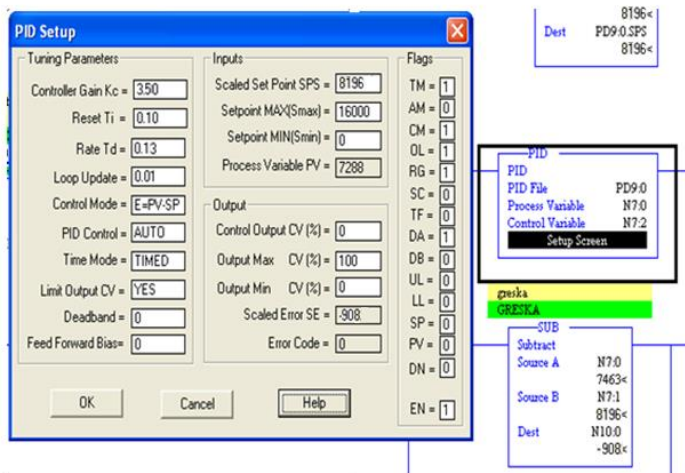


Fig. 19 PID command of the PLC controller

6. EXPERIMENTAL RESULTS

The Fig. 20 shows the PID controller control signal values and the difference between the setpoint and actual position for the dancer performed in the lower end position values of PLC memory register.

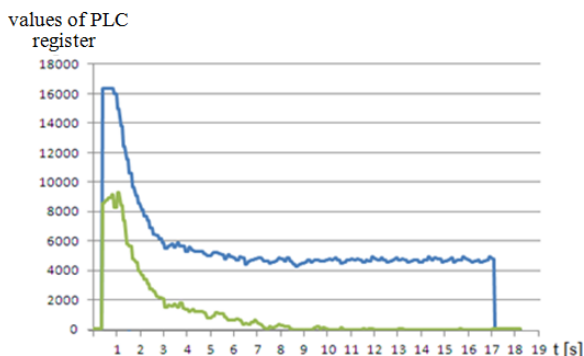


Fig. 20 Control signal (blue) characteristic and the difference between the setpoint and the actual dancer position (green) when the dancer positioning in lower position (16384 units = 10V, $x=0,6\text{m}$ or 8192 units)

The Fig. 21 shows the values of the control signal of the PID regulator and the difference between the setpoint and the actual dancer position performed in the middle of the setpoint and lower position.

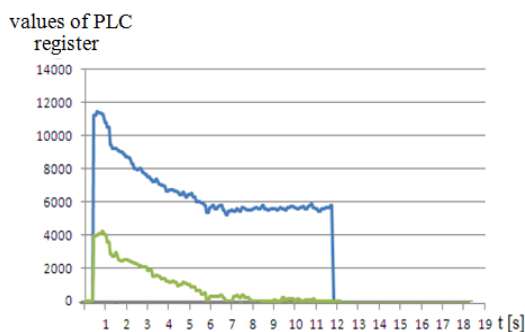


Fig. 21 Control signal (blue) characteristic and the difference between the setpoint and the actual (green) when the dancer positioning in the middle of the setpoint and lower position (16384 units = 10V, $x=0,6\text{m}$ or 8192 units)

Figures 22 and 23 show the values of the control signal, the setpoint and actual values of the position for the dancer in the event of a random disturbance. The accidental disturbance was performed by intentionally stopping and starting the part of the line that delivers the cable to the dancer and the winder.

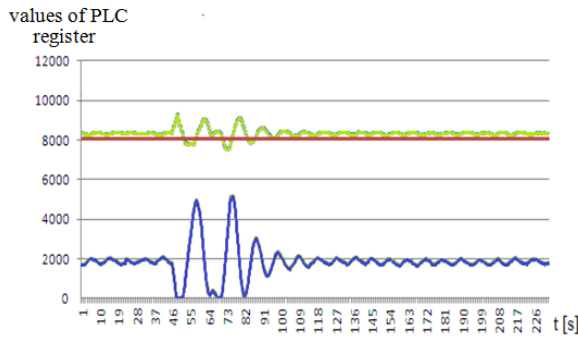


Fig. 22 Characteristics of the control signal (blue), setpoint (red) and actual values of the position (green) for the dancer in the event of an accidental disturbance (16384 units = 10V, $x=0,6m$ or 8192 units)

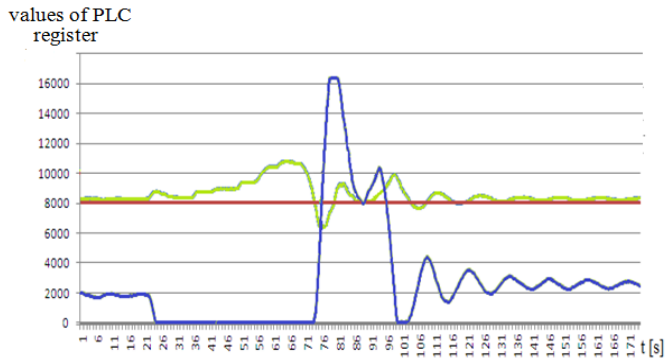


Fig. 23 Characteristics of the control signal (blue), setpoint (red) and actual values of the position (green) for the dancer in the event of an accidental disturbance (16384 units = 10V, $x=0,6m$ or 8192 units)

7. CONCLUSION

The main problem in regulating the winder speed or current dancer’s position in industrial conditions arises due to the limit of resource restricting the quality regulation. As the high accuracy of the regulation is not an absolute imperative, some PLC controllers of reputable manufacturers are used for the PID regulation. The proposed method for regulating the current position of the winder’s dancer for PID with differential effect per position signal gives satisfying results.

APPENDIX

The Table 1 contains DC motor’s parameters, the Table 2 gives dancer model’s parameters.

Table 1 Parameters of the DC motor

P	5 HP
R_a	2.581 Ω
L_a	0.0281 H
V_a	240 V
R_f	281.3 Ω
L_f	156 mH
V_f	300 V
J_m	0.0221 kgm^2
B_m	0.002953 Nms
K_e	1.25 Vs/rad
K_m	0.516 Nm/A
n	1750 rpm

Table 2 Parameters of the dancer's model

m	1.4 kg
B	17.789 Ns/cm
k_1	1.5 N/cm
k_2	1.172 N/cm ³

Acknowledgement: *This work has been supported by the Ministry of Education, Science and Technological Development of the Republic of Serbia.*

REFERENCES

- [1] G. Brandenburg, "New mathematical model for web tension and register error", in *Proceedings of the 3rd International IFAC Conference On Instrumentation And Automation In The Paper, Rubber and Plastics*, Brussels, Belgium, vol. 1, 1976, pp. 411–438.
- [2] G. E. Young and K. N. Reid, "Lateral and longitudinal dynamic behavior and control of moving webs", *Journal of Dynamic Systems, Measurement, and Control*, vol. 115, pp 309-317, 1993. doi: 10.1115/1.2899071
- [3] K. N. Reid, K.-H. Shin, and K.-C. Lin, "Variable-gain control of longitudinal tension in a web transport system", *Web Handling*, vol. 149, pp. 87–100, 1992.
- [4] D. Koenig, , *Practical Control Engineering: A Guide for Engineers, Managers, and Practitioners*, McGraw-Hill Education, 2009.
- [5] SimoreG DC-Master 6RA70 Series Operating Instructions Microprocessor-Based Converters from 6kW to 2500kW for Variable-Speed DC Drives, [Online]. Available: https://cache.industry.siemens.com/dl/files/212/22220212/att_26325/v1/C98130-A1256-A002-14-7619.pdf.
- [6] R. V. Dwivedula, Y. Zhu, and P. R. Pagilla, "Characteristics of active and passive dancers: a comparative study", *Control Engineering Practice*, vol. 14, no. 4, pp. 409–423, 2006. doi: 10.1016/j.conengprac.2005.02.003
- [7] Kepserverex manual, [Online]. Available: <https://www.kepware.com/getattachment/2745a0a9-079a-4630-b15c-8081aba1a91d/kepserverex-manual.pdf>
- [8] F. G. Martins, "Tuning PID controllers using ITAE criterion", *International Journal of Engineering Education*, vol. 21, no. 5, 2005.
- [9] S. Daley and G. Liu, "Optimal PID tuning using direct search algorithms", *IET Computing & Control Engineering Journal*, vol. 10, no. 2, pp. 51–56, 1999. doi: 10.1049/cce:19990203
- [10] Mathworks, [Online]. Available: <https://www.mathworks.com/matlabcentral/mlc-downloads/downloads/submissions/18674/versions/1/previews/html/optimalpidtuning.html>
- [11] D. P. Radusinović, *Numeričke metode*, Akademska misao, Beograd, 2004.

- [12] J. H. Matthews, *Simpson's 3/8 Rule for Numerical Integration, Numerical Analysis-Numerical Methods Project*, California State University, Fullerton, USA, 2004.
- [13] K. J. Astrom and T. Hagglund, "The future of PID control", *Control Engineering Practice*, vol. 9, no. 11, 2001, pp. 1163–1175, 2001. doi: 10.1016/S0967-0661(01)00062-4
- [14] MicroLogix™ 1200 and MicroLogix 1500 Programmable Controllers, [Online]. Available: https://literature.rockwellautomation.com/idc/groups/literature/documents/rm/1762-rm001_en-p.pdf
- [15] I. Kocić, P. Đekić, A. Milovanović, D. Antić, S. S. Nikolić, and N. Danković, "Application of KEPServerEX applications for acquisition and supervision of production processes", in *Proceedings of the XV International Conference on Systems, Automatic Control and Measurements, SAUM 2021*, Niš, Serbia, September 09.-10., 2021., pp. 17–20.
- [16] I. Kocić, S. S. Nikolić, A. Milovanović, P. Đekić, and N. Danković, "Sequential control of water level in tanks and pumps from remote location using PROFINET network", *Proceedings of the 9th Small Systems Simulation Symposium, SSSS 2022*, Niš, Serbia, February 28.–March 02., 2022., pp. 90–97.

OPTIMIZATION AND PERFORMANCE ANALYSIS OF THE 30-BIT FIXED-POINT DIGITAL FORMAT

UDC ((681.586+621.391):004.4)

Milan Dinčić¹, Zoran Perić², Dragan Denić¹

¹University of Niš, Faculty of Electronic Engineering, Department of Measurements,
Republic of Serbia

²University of Niš, Faculty of Electronic Engineering, Department of Telecommunications,
Republic of Serbia

Abstract. *The 32-bit floating-point format (FP32) is standardly used for digital representation of data in computers, providing high quality of digital representation in a very wide dynamic range of data. However, the FP32 format has a very high computational complexity, requiring the use of expensive and powerful hardware, as well as high energy consumption. Hence, the implementation of the FP32 format on devices such as smart sensors, embedded and edge devices that have limited hardware resources becomes very problematic. On the other hand, the fixed-point format has significantly less computational complexity, consumes less power, requires less area on chip and provides faster calculations than the floating-point format, being much more suitable for implementation on devices with limited hardware resources.*

The main goal of this paper is to find a fixed-point format that will be a good replacement for the FP32 format, in the sense that it provides the same performance as the FP32 format and at the same time significantly reduces the computational complexity. Therefore, the paper considers the 30-bit fixed-point format, optimizes the value of its parameters and evaluates its performance, using the analogy between the fixed-point digital representation and uniform quantization. As the main result, the paper shows that the 30-bit fixed-point format can achieve a better quality (i.e. higher SQNR) of digital representation for 3.352 dB compared to the FP32 format, saving at the same time 2 bits per each piece of data (which can be a significant saving for a large amount of data) and significantly reducing the complexity of the implementation. Therefore, the proposed 30-bit fixed-point format can be successfully used as a replacement for the FP32 format on devices with limited resources.

Key words: *Fixed-point digital format, floating-point digital format, uniform quantization, piecewise uniform quantization, smart sensors, resource-constrained devices*

Received July 26, 2022 / Accepted October 17, 2022

Corresponding author: Milan Dinčić

University of Niš, Faculty of Electronic Engineering, Department of Measurements, Aleksandra Medvedeva 14,
18000 Niš, Republic of Serbia

E-mail: milan.dincic@elfak.ni.ac.rs

I. INTRODUCTION

Today there is the dominance of digital systems that use digital representation of data. The main condition that the digital representation must satisfy is to ensure the appropriate accuracy of the digitized data (usually increasing the number of bits in the digital representation increases the accuracy of the representation). Also, it is important for the digital representation to be adapted to the dynamic range of data, i.e. to ensure the required accuracy in the entire dynamic range of data (this is very important for data with a wide dynamic range, i.e. with a large difference between the smallest and the largest value). However, due to the constantly increasing amount of data, it is very important for the digital representation to be efficient in terms of providing the required accuracy of the representation with as few bits as possible.

There are two basic types of digital formats for data representation: the floating-point format [1, 2] and the fixed-point format. The floating-point format, defined by the IEEE 754 standard [1], is dominantly used for the digital representation of data in computers since it provides a high quality of digital representation in a very wide dynamic range of data (from very small to very large data values). However, the main disadvantage of the floating-point format is the high computational complexity, which requires the use of expensive and powerful hardware. Another negative consequence of the floating-point processing is high energy consumption [3]. While powerful computers can easily support the floating-point format, its implementation on devices such as smart sensors, embedded and edge devices that have limited hardware resources (limited processing power, limited energy since they are mostly battery-powered, as well as limited memory capacity) becomes very problematic. In fact, many embedded and edge devices do not support the floating-point format at all [4].

On the other hand, the fixed-point format has significantly less computational complexity, consumes less power, requires less area on chip and provides faster calculations than the floating-point format [5, 6, 7], being much more suitable for implementation on devices with limited hardware resources.

A particularly current trend is the implementation of DNN (deep neural networks) [8] on smart sensors and edge devices. Since DNN parameters are standardly represented in the 32-bit floating-point format (FP32), the possibility of implementing DNN on these devices is significantly limited. One very effective way to overcome this problem is to represent the DNN parameters in the fixed-point format. Based on all the above, the analysis and optimization of the fixed-point format becomes a very important research topic.

The main goal of this paper is to find a fixed-point format that will be a good replacement for the FP32 format, in the sense that it provides the same performance as the FP32 format and at the same time significantly reduces the computational complexity.

In the paper [9], an analogy was established between the floating-point digital format and piecewise uniform quantization, showing that the floating-point format can be considered as a piecewise uniform quantizer. Also, in the paper [10], an analogy between the fixed-point format and uniform quantization was established, showing that the fixed-point digital format can be considered as a uniform quantizer. These analogies between digital formats and quantizers are very important because they allow us to express the performance of digital formats through an objective quantizer performance, such as distortion and signal-to-quantization noise ratio (SQNR).

As the performance of the quantizers depends on the probability density function (PDF) of the input data, the accuracy of the digital representation also depends on the PDF of the input data. This paper considers the Laplacian PDF, which is widely used for statistical modeling of different types of data [11, 12].

In this paper, the 32-bit floating-point (FP32) digital format is considered first. The analogy between the FP32 format and the 32-bit piecewise uniform quantizer is explained; then, using this analogy, the quality of the FP32 format is expressed by the SQNR of the 32-bit piecewise uniform quantizer. It is shown that the quality of digital representation of the FP32 format corresponds to the SQNR value of 151.934 dB. Since the FP32 format is robust [9], this value of SQNR is constant in a very wide range of variance of the input data.

The key part of the paper is the optimization of the 30-bit fixed-point format in terms of determining the optimal value of the parameter n which represents the number of bits used to encode the integer part of real numbers, using an analogy with the 30-bit uniform quantizer. An iterative algorithm for the calculation of the optimal value of the parameter n is defined and it is shown that the optimal value is $n = 5$ for data with the unit variance. Using the mentioned analogy, the performance of the 30-bit fixed-point format is analyzed, showing that it achieves a quality of digital representation equivalent to the SQNR value of 155.286 dB for data with the unit variance. As the fixed-point format is not robust [10], the SQNR value will decrease if the variance of the input data deviates from 1. However, if an adaptation is performed as suggested in the paper, the 30-bit fixed-point format will achieve constant SQNR of 155.286 dB in a very wide range of variance, similar to the FP32 format.

Hence, the main contribution of this paper is the design of the 30-bit fixed-point format that achieves a better quality (i.e. higher SQNR) of digital representation for 3.352 dB in a wide range of data variance compared to the FP32 format, saving at the same time 2 bits per each piece of data (which can be a significant saving for a large amount of data) and significantly reducing the complexity of the implementation. Therefore, the proposed 30-bit fixed-point format can be successfully used as a replacement for the FP32 format on devices with limited resources.

2. THE 32-BIT FLOATING POINT QUANTIZER

We will firstly consider the 32-bit floating-point (FP32) binary format, standardly used for the binary representation of data. A real number x can be represented in the FP32 format as:

$$x = (se_1e_2\dots e_8 m_1m_2\dots m_{23})_2. \quad (1)$$

In the binary representation (1) we have one bit 's' intended for encoding the sign of the real number x , 8 bits ($e_1e_2\dots e_8$) intended for encoding the exponent and 23 bits ($m_1m_2\dots m_{23}$) representing the significand. The exponent E is calculated as:

$$E = \sum_{i=1}^8 e_i 2^{8-i} \quad (2)$$

and can take values from 0 to 255. A real number x represented in the FP32 format (1) is calculated as:

$$x = (-1)^s \cdot (1.m_1 \dots m_{23})_2 \cdot 2^{E-127} = (-1)^s \cdot (1.m_1 \dots m_{23})_2 \cdot 2^{E^*}, \quad (3)$$

where $E^* = E - 127$ represents the biased exponent that can take values from -127 to 128. However, according to the IEEE 754 standard [1], the two end values ($E^* = -127$ and $E^* = 128$) are reserved for special purposes, hence the values from $E^* = -126$ to $E^* = 127$ are available for the binary representation of numbers. It is valid that:

$$(1.m_1 \dots m_{23})_2 = 1 + \sum_{i=1}^{23} m_i 2^{-i} = 1 + 2^{-23} \sum_{i=1}^{23} m_i 2^{23-i} = 1 + \frac{M}{2^{23}}, \quad (4)$$

whereby the parameter M , defined as:

$$M = \sum_{i=1}^{23} m_i 2^{23-i} \quad (5)$$

can take values from 0 to $2^{23} - 1$. Based on (3) and (4), a real number x represented in the FP32 format is calculated as:

$$x = (-1)^s \cdot (1.m_1 \dots m_{23})_2 \cdot 2^{E-127} = (-1)^s \cdot 2^{E^*} \left(1 + \frac{M}{2^{23}} \right). \quad (6)$$

For each positive number represented in the FP32 format, there is a corresponding negative counterpart, meaning that the FP32 format is symmetrical about zero. The maximal positive number that can be represented in the FP32 format (for $E^* = 127$ and $2^{23} - 1$) is

$$x_{\max} = 2^{127} \left(1 + \frac{2^{23} - 1}{2^{23}} \right) = 2^{127} \left(2 - \frac{1}{2^{23}} \right) = 2^{128} \left(1 - \frac{1}{2^{24}} \right) \approx 2^{128}. \quad (7)$$

Due to the symmetry, the maximal negative number represented in the FP32 format is -2^{128} .

Let us consider the positive numbers in the FP32 format. There are 254 values of E^* ($-126 \leq E^* \leq 127$) and for each value of E^* there are 2^{23} values of M ($0 \leq M \leq 2^{23} - 1$). For each value of E^* we have a group of 2^{23} numbers (each of them corresponding to one value of M). Therefore, in total we have 254 groups (whereby each group corresponds to one value of E^*) with 2^{23} numbers within each of them. Let us consider a group G_{E^*} of 2^{23} adjacent numbers for some arbitrary value of E^* . Let $x_{E^*,i}$ denote the i -th number in that group obtained for $M = i$ ($0 \leq i \leq 2^{23} - 1$). According to (6) we have that:

$$x_{E^*,i} = 2^{E^*} \left(1 + \frac{i}{2^{23}} \right). \quad (8)$$

The distance between two adjacent numbers within the group G_{E^*} is

$$\Delta_{E^*} = x_{E^*,i+1} - x_{E^*,i} = 2^{E^*} \left(1 + \frac{i+1}{2^{23}} \right) - 2^{E^*} \left(1 + \frac{i}{2^{23}} \right) = 2^{E^*-23}. \quad (9)$$

Numbers from the group G_{E^*} belongs to the interval $S_{E^*} = [2^{E^*}, 2^{E^*+1})$.

In total, we have 254 groups of 2^{23} numbers in the positive part; the numbers from one group have the same value of E^* , being uniformly distributed in the segment $S_{E^*} = [2^{E^*}, 2^{E^*+1})$ with the step-size $\Delta_{E^*} = 2^{E^*-23}$. Since the step-size Δ_{E^*} depends on E^* , it is obvious that the step-size has different values in different groups. A symmetrical structure exists in the negative part.

We can see that the structure of the FP32 format corresponds to the structure of a symmetrical 32-bit piecewise uniform quantizer with the support region $[-x_{\max}, x_{\max}]$, which consists of 254 segments $[2^{E^*}, 2^{E^*+1})$ in the positive part ($-126 \leq E^* \leq 127$), whereby the uniform quantization with 2^{23} quantization levels and with quantization step-size $\Delta_{E^*} = 2^{E^*-23}$ is performed within each segment. This 32-bit piecewise uniform quantizer that corresponds to the structure of the FP32 format will be called *the 32-bit floating-point quantizer*. This analogy between the FP32 representation and the 32-bit floating-point quantizer will allow us to determine the quality of the FP32 binary representation, based on the objective performance (distortion D and SQNR) of the 32-bit floating-point quantizer.

During the quantization, an irreversible error is made, which is expressed by distortion. For the 32-bit piecewise floating-point quantizer, the distortion D is calculated as:

$$D = 2 \sum_{E^*=-126}^{127} \frac{\Delta_{E^*}^2}{12} P_{E^*} + 2 \int_{x_{\max}}^{+\infty} (x - x_{\max})^2 p(x) dx. \quad (10)$$

Multiplication by 2 in the expression (10) serves to incorporate the distortion in the negative part, which is the same as the distortion in the positive part due to the symmetry. The first term in (10), expressed in the form of a sum, represents the granular distortion that corresponds to the quantization error caused by quantizing data belonging to the support region of the quantizer. The granular distortion of the 32-bit piecewise uniform quantizer is expressed in the form of a sum, where each member of the sum represents the distortion of the uniform quantization in one of 254 segments. P_{E^*} represents the probability that the input data belongs to the segment $[2^{E^*}, 2^{E^*+1})$. The probability P_{E^*} is defined as:

$$P_{E^*} = \int_{2^{E^*}}^{2^{E^*+1}} p(x) dx, \quad (11)$$

where $p(x)$ represents the probability density function (PDF) of the input data.

The second term in the expression (10) represents the overload distortion that corresponds to the quantization error caused by quantizing data outside the support region of the quantizer. We can see that the overload distortion also depends on the PDF of the input data. In general, the performance of any quantizer depends on the PDF of the input data, i.e. we need to know the PDF of the input data to determine the performance of the quantizer. In this paper, we will consider the Laplacian PDF which is widely used for statistical modeling of many types of data [11, 12]. The Laplacian PDF is defined by the following expression [11]:

$$p(x) = \frac{1}{\sqrt{2}\sigma} \exp\left(-\frac{|x|\sqrt{2}}{\sigma}\right), \quad (12)$$

where σ^2 represents the variance of the input data. Quantizers are usually designed for the unit variance ($\sigma^2 = 1$), hence we will below consider the Laplacian PDF with the unit variance defined as:

$$p(x) = \frac{1}{\sqrt{2}} \exp(-|x|\sqrt{2}). \quad (13)$$

The probability P_{E^*} for $p(x)$ defined by (13) is calculated as:

$$P_{E^*} = \frac{1}{2} \left(\exp\left(-2^{E^* + \frac{1}{2}}\right) - \exp\left(-2^{E^* + \frac{3}{2}}\right) \right). \quad (14)$$

The expression for the overload distortion for $p(x)$ defined by (13) becomes:

$$D_{ov} = \exp(-\sqrt{2}x_{\max}) = \exp(-\sqrt{2} \cdot 2^{128}). \quad (15)$$

Substituting (11), (14) and (15) into (10), the expression for the distortion of the 32-bit floating-point quantizer becomes:

$$D = \sum_{E^*=-126}^{127} \frac{1}{12} \cdot 2^{2E^*-46} \cdot \left(\exp\left(-2^{E^* + \frac{1}{2}}\right) - \exp\left(-2^{E^* + \frac{3}{2}}\right) \right) + \exp(-\sqrt{2} \cdot 2^{128}). \quad (16)$$

Quality of the quantization is expressed by SQNR (signal-to-quantization noise ratio), which is defined as

$$\text{SQNR [dB]} = 10 \log_{10} \frac{\sigma^2}{D}. \quad (17)$$

For $\sigma^2 = 1$ and for the distortion defined by (16), the expression for the SQNR of the 32-bit floating-point quantizer becomes:

$$\begin{aligned} \text{SQNR [dB]} = \\ -10 \log_{10} \left[\sum_{E^*=-126}^{127} \frac{2^{2E^*-46}}{12} \cdot \left(\exp\left(-2^{E^* + \frac{1}{2}}\right) - \exp\left(-2^{E^* + \frac{3}{2}}\right) \right) + \exp(-\sqrt{2} \cdot 2^{128}) \right]. \end{aligned} \quad (18)$$

After calculation we obtain that SQNR = 151.934 dB.

The 32-bit floating-point quantizer is very robust since it has a constant SQNR over a very wide range of variance [9]. This means that even if the variance of the input data deviates significantly from $\sigma^2 = 1$, the SQNR will keep the same value, i.e. the quality of the FP32 representation will remain the same.

3. THE 30-BIT FIXED POINT QUANTIZER

A real number x is represented in the 30-bit fixed-point binary representation as:

$$x = (s a_{n-1} a_{n-2} \dots a_1 a_0 . a_{-1} \dots a_{-m})_2. \quad (19)$$

The binary representation (19) consists of one bit ‘ s ’ intended for encoding of the sign of x ($s = 0$ if $x > 0$ and $s = 1$ if $x < 0$), n bits ($a_{n-1}a_{n-2}\dots a_1a_0$) intended for encoding of the integer part of x and m bits ($a_{-1}\dots a_{-m}$) intended for encoding of the fractional part of x . It holds that $n + m + 1 = 30$, therefore, we have that:

$$m = 29 - n . \quad (20)$$

The main issue related to the fixed-point format is how to choose values of parameters n and m . According to (20), if we find the optimal value of n , we can easily calculate the optimal value of m .

The fixed-point binary format is a weighted format, whereas each bit a_i ($i = -m, \dots, n-1$) has the weight of 2^i . Using this fact, we can calculate the real number x represented in the 30-bit fixed-point binary format as:

$$x = (-1)^s \sum_{i=-m}^{n-1} a_i 2^i . \quad (21)$$

For each positive number represented in the fixed-point format, there is a negative counterpart. Hence, the fixed-point format is symmetrical about zero. The number 0 is represented with all bits equal to 0. The largest positive number that can be represented in the 30-bit fixed-point format is:

$$x_{\max} = (1\dots 1.1\dots 1)_2 = \sum_{i=-m}^{n-1} 2^i = 2^{-m} \sum_{i=0}^{n+m-1} 2^i = 2^{-m} (2^{n+m} - 1) = 2^n - 2^{-m} . \quad (22)$$

Using (20) it is obtained that:

$$x_{\max} = 2^n - 2^{n-29} = 2^n \left(1 - \frac{1}{2^{29}} \right) \approx 2^n . \quad (23)$$

Due to the symmetry, the largest negative number that can be represented is -2^n .

Let us consider the first few positive numbers represented in the 30-bit fixed point format:

$$\begin{aligned} (0..0.0\dots 01)_2 &= 2^{-m} , \\ (0..0.0\dots 010)_2 &= 2^{-(m-1)} = 2 \cdot 2^{-m} , \\ (0..0.0\dots 011)_2 &= 2^{-(m-1)} + 2^{-m} = 3 \cdot 2^{-m} , \text{ etc.} \end{aligned}$$

It is obvious that the numbers represented in the 30-bit fixed point format are uniformly distributed (i.e. equidistant) discrete numbers, whereas the distance between adjacent numbers is $\Delta = 2^{-m}$. Hence, we can conclude that the 30-bit fixed-point format represents uniformly distributed discrete numbers from the range $[-x_{\max}, x_{\max}] = [-2^n, 2^n]$, with the step-size $\Delta = 2^{-m}$. According to (20), the step-size Δ can be written as:

$$\Delta = 2^{n-29} . \quad (24)$$

Based on the above, the 30-bit fixed-point representation can be considered as a 30-bit uniform quantizer with the following parameters: the maximal amplitude $x_{\max} = 2^n$, the support region $[-2^n, 2^n]$ and the quantization step-size $\Delta = 2^{n-29}$. This uniform quantizer that corresponds to the 30-bit fixed-point representation will be called *the 30-bit fixed-point quantizer*. This analogy between the 30-bit fixed-point representation and the 30-bit

fixed-point uniform quantizer will allow us to assess the quality of the 30-bit fixed-point representation based on the performance of the 30-bit fixed-point quantizer. Therefore, we will analyze the performance of the 30-bit fixed-point quantizer below.

Based on the quantization theory, the distortion of the 30-bit fixed-point quantizer can be expressed as [11]:

$$D = \frac{\Delta^2}{12} + 2 \int_{x_{\max}}^{+\infty} (x - x_{\max})^2 p(x) dx. \quad (25)$$

The first term in the expression (25) represents the granular distortion while the second term in (25) represents the overload distortion. For the unit-variance Laplacian PDF defined with (13), the overload distortion becomes:

$$D_{ov} = 2 \int_{x_{\max}}^{+\infty} (x - x_{\max})^2 p(x) dx = \exp(-\sqrt{2} \cdot x_{\max}). \quad (26)$$

Substituting (26) in (25), we obtain the following expression for the distortion of the 30-bit fixed-point quantizer:

$$D = \frac{\Delta^2}{12} + \exp(-\sqrt{2} \cdot x_{\max}). \quad (27)$$

Using (24) and (23), the distortion D can be expressed as a function of the parameter n , in the following way:

$$D(n) = \frac{2^{2n-58}}{12} + \exp(-\sqrt{2} \cdot 2^n) = \frac{2^{2n-58}}{12} + \exp\left(-2^{n+\frac{1}{2}}\right). \quad (28)$$

The quality of the 30-bit fixed-point quantization is expressed by an objective measure SQNR (signal-to-quantization noise ratio), which is defined in the following way, being also a function of the parameter n :

$$\text{SQNR}(n) [\text{dB}] = -10 \cdot \log_{10}(D(n)) = -10 \cdot \log_{10}\left(\frac{2^{2n-58}}{12} + \exp\left(-2^{n+\frac{1}{2}}\right)\right). \quad (29)$$

The performance of the 30-bit fixed-point quantizer is expressed by objective measures: by the distortion D and by SQNR.

Our goal is to optimize the value of the parameter n in a way to maximize the quality of the 30-bit fixed-point representation. Because of the analogy between the 30-bit fixed-point representation and the 30-bit fixed-point quantizer, maximizing the quality of the 30-bit fixed-point format is equivalent to achieving the best performance of the 30-bit fixed-point quantizer. Therefore, the optimization of the value of the parameter n can be performed by maximizing the SQNR or minimizing the distortion D of the 30-bit fixed-point quantizer. Thus, the analogy between the 30-bit fixed-point format and the 30-bit fixed-point quantizer allows us to optimize the 30-bit fixed-point representation using objective quality measures (D and SQNR) of the 30-bit fixed-point quantizer.

In order to minimize the distortion D , we will find the first derivative of the function $D(n)$:

$$\frac{dD(n)}{dn} = 2^{n+\frac{1}{2}} \ln 2 \cdot \left(\frac{2^{-58}}{12} 2^{n+\frac{1}{2}} - \exp\left(-2^{n+\frac{1}{2}}\right) \right). \quad (30)$$

From the condition $\frac{dD(n)}{dn} = 0$ the following equation is obtained:

$$\frac{2^{-58}}{12} 2^{n+\frac{1}{2}} - \exp\left(-2^{n+\frac{1}{2}}\right) = 0. \quad (31)$$

Let us define the following substitution:

$$t = 2^{n+\frac{1}{2}}. \quad (32)$$

The equation (31) becomes:

$$\exp(-t) = \frac{2^{-58}}{12} t. \quad (33)$$

By logarithmization of both sides of the equation (33), it is obtained that:

$$t = -\ln\left(\frac{2^{-58}}{12} t\right) = \ln\left(\frac{12 \cdot 2^{58}}{t}\right) = \ln(12) + 58 \cdot \ln 2 - \ln t = 42.6874 - \ln t. \quad (34)$$

Based on (34), we can define the following iterative process for calculating the optimal value of the parameter t :

$$t_{i+1} = 42.6874 - \ln t_i. \quad (35)$$

where t_i denotes the value of t in the i -th iteration.

Let us arbitrarily choose the value of the starting point of the iterative process as $t_0 = 20$. The values of the parameter t in the first few iterations are: $t_1 = 39.6917$, $t_2 = 39.0063$, $t_3 = 39.0237$, $t_4 = 39.0233$, $t_5 = 39.0233$, $t_6 = 39.0233$. We can see that the iterative process very quickly (after 4 iterations) reaches the value 39.0233 and remains at that value. We can say that the iterative process (35) converges to the value 39.0233, therefore the optimal value of the parameter t is $t_{opt} = 39.0233$. Based on (32), the optimal value of the parameter n is calculated as:

$$n_{opt} = \log_2(t_{opt}) - \frac{1}{2} = 4.786. \quad (36)$$

However, the parameter n must be an integer. Since n_{opt} is between 4 and 5, it is clear that the optimal integer value of the parameter n must be 4 or 5. According to (29), $\text{SQNR}(n=4) = 98.270$ dB and $\text{SQNR}(n=5) = 155.286$ dB. Since $\text{SQNR}(n=5) > \text{SQNR}(n=4)$, it is obvious that the optimal value of the parameter n for the 30-bit fixed-point format is $n = 5$. Based on (20), (23) and (24), the optimal values of the parameters of the 30-bit fixed-point quantizer are:

$$n = 5, m = 24, x_{\max} = 2^n = 32 \text{ and } \Delta = 2^{-m} = 2^{-24}. \quad (37)$$

The SQNR of the 30-bit fixed-point quantizer with parameters defined by (37) is 155.286 dB.

Let us calculate SQNR of the 30-bit fixed-point quantizer for several values of the parameter n close to the optimal value $n = 5$, which is shown in Table 1. We can see from Table 1 that the wrong choice of the value of the parameter n drastically reduces the SQNR, therefore reducing the 30-bit fixed-point representation. This fact confirms the importance of determining the optimal value of the parameter n .

Table 1 SQNR of the 30-bit fixed-point quantizer for different values of the parameter n

n	SQNR [dB]
3	49.135
4	98.270
5	155.286
6	149.266
7	143.245

The fixed-point format has significantly less robustness than the floating-point format [10], so the SQNR value will decrease as the value of the data variance moves away from 1. However, by applying well-known adaptation methods (such as the forward adaptation, which involves grouping data into blocks, calculating the variance σ^2 of each block, dividing data in the block by σ to normalize the variance of the block to 1, and storing σ in order to subsequently reconstruct the original data values) [11], the SQNR of the 30-bit fixed-point format can easily maintain a constant value of 155.286 dB over a very wide range of variance of the input data. Increasing of the processing time due to adaptation depends on the size of the block of data for adaptation, therefore the size of the block should be optimized taking into account the allowed processing time and the required quality of adaptation for a specific application. The proposed adaptation techniques have been successfully used in real-time applications for a long time (e.g. speech and image transmission [11]), showing that the increasing of complexity and processing time due to the adaptation techniques is not critical.

We can see that the adaptive 30-bit fixed-point format achieves for 3.352 dB higher SQNR compared to the 32-bit floating-point format (FP32), with a saving of 2 bits per each data element. At the same time, the 30-bit fixed-point format has significantly less complexity compared to the FP32 format. Increasing of SQNR contributes to the quality of digital data representation. In the context of DNN, there is a direct correlation between SQNR of data representation and prediction/classification accuracy; hence, the increasing the SQNR of 3,352 dB may have a certain positive effect on the prediction/classification accuracy.

7. CONCLUSION

The paper considered the 30-bit fixed-point format using an analogy with the 30-bit uniform quantizer in terms of determining the optimal value of the parameter n which represents the number of bits used to encode the integer part of real numbers, using an analogy with the 30-bit uniform quantizer. An iterative algorithm was defined for optimization of the parameter n (the number of bits used to encode the integer part of real numbers). It was shown that the optimal value of n is 5 for data with the unit variance. Also, it was shown that the 30-bit fixed-point format could achieve a quality of digital representation equivalent to the SQNR

value of 155.286 dB. By performing some of the well-known adaptation techniques (such as the forward adaptation), the mentioned value of SQNR can be kept constant in a very wide range of variance.

The main conclusion of the paper is that the 30-bit fixed-point format can achieve a better quality (i.e. higher SQNR) of digital representation for 3.352 dB in a wide range of data variance compared to the FP32 format, saving at the same time 2 bits per each piece of data (which can be a significant saving for a large amount of data) and significantly reducing the complexity of the implementation. Therefore, the proposed 30-bit fixed-point format can be successfully used as a replacement for the FP32 format on devices with limited resources.

Acknowledgement: *This work has been supported by the Science Fund of the Republic of Serbia (Grant No. 6527104, AI- Com-in-AI) as well as by the Ministry of Education, Science and Technological Development of the Republic of Serbia (projects TR-32045 and III-42009).*

REFERENCES

- [1] IEEE Standard for Floating-Point Arithmetic IEEE 754-2019, <https://standards.ieee.org/ieee/754/6210/>.
- [2] D. Zoni, A. Galimberti and W. Fornaciari, "An FPU design template to optimize the accuracy-efficiency-area trade-off", *Sustainable Computing: Informatics and Systems*, vol. 29, part A, March 2021, doi: 10.1016/j.suscom.2020.100450.
- [3] G. Tagliavini, S. Mach, D. Rossi, A. Marongiu and L. Benini, "A transprecision floating-point platform for ultra-low power computing", *2018 Design, Automation Test in Europe Conference Exhibition (DATE)*, March 2018, pp. 1051–1056.
- [4] D. Cattaneo, A. Di Bello, S. Cherubin, F. Terraneo and G. Agosta, "Embedded Operating System Optimization through Floating to Fixed Point Compiler Transformation", *2018 21st Euromicro Conference on Digital System Design (DSD)*, Prague, Czech Republic, 29-31 August 2018, doi: 10.1109/DSD.2018.00042.
- [5] MathWorks. Benefits of fixed-point hardware. [Online]. Available: <https://de.mathworks.com/help/fixedpoint/g/benefitsof-fixed-point-hardware.html>.
- [6] NI. (2019) Advantages of fixed-point numbers on hardware. [Online]. Available: <https://www.ni.com/documentation/en/labview/latest/datatypes/advantages-fixed-point-numbers/>.
- [7] R. T. Syed, M. Ulbricht, K. Piotrowski, and M. Krstic, "Fault Resilience Analysis of Quantized Deep Neural Networks", *2021 IEEE 32nd International Conference on Microelectronics (MIEL)*, Niš, Serbia, September 12-14, 2021, pp. 275-279, doi: 10.1109/MIEL52794.2021.9569094.
- [8] A. Zhang, Z. -C. Lipton, M. Li and A. -J. Smola, "Dive into Deep Learning", Amazon Science, (2020).
- [9] Z. Peric, M. Savic, M. Dincic, N. Vucic, D. Djosic and S. Milosavljevic, "Floating point and fixed point 32-bits quantizers for quantization of weights of neural networks", *12th International Symposium on Advanced Topics in Electrical Engineering (ATEE)*, Bucharest, Romania, March 2021, pp. 1-4, doi: 10.1109/ATEE52255.2021.9425265.
- [10] Z. Perić, A. Jovanović, M. Dinčić, M. Savić, N. Vučić and A. Nikolić, "Analysis of 32-bit Fixed Point Quantizer in the Wide Variance Range for the Laplacian Source", *2021 15th International Conference on Advanced Technologies, Systems and Services in Telecommunications (TELSIKS)*, Niš, Serbia, 20-22 October 2021, doi: 10.1109/TELSIKS52058.2021.9606251.
- [11] N. C. Jayant and P. Noll, "Digital Coding of Waveforms: Principles and Applications to Speech and Video", Prentice Hall, (1984).
- [12] J. Nikolić, D. Aleksić, Z. Perić and M. Dinčić, "Iterative Algorithm for Parameterization of Two-Region Piecewise Uniform Quantizer for the Laplacian Source", *Mathematics*, vol. 9, no. 23: 3091, 2021, doi: 10.3390/math9233091.

OFDM LOW COMPLEXITY CHANNEL ESTIMATION USING TIME-FREQUENCY ADJUSTABLE WINDOW FUNCTIONS

UDC ((004.3/.4+629.783):517.518.5)

Veljko Stanković, Zoran Perić

University of Niš, Faculty of Electronic Engineering, Department of Telecommunications,
Republic of Serbia

Abstract. *In this paper, we introduce a low complexity algorithm for estimation of the channel transfer function in the OFDM communication system that is using a scattered pilot symbol grid. Although, the use of the scattered pilot grid enables implementation of the flexible, and adaptive radio interface, it suffers from a high estimation error at the edges of the symbol sequence. Due to the sampling in time, and frequency, the signal is circularly expanded in both domains, and this has to be taken into account when the signal is processed. The proposed algorithm is shaping the pilot symbol estimates in time, and frequency domain, such that the aliasing in both domains are reduced or eliminated. We achieve a significant reduction of the estimation error, with a linear increase in computational complexity.*

Key words: *Channel estimation, window functions, signal processing, Discrete Fourier transform*

1. INTRODUCTION

Modern communication systems require accurate channel state information estimates in order to perform a coherent detection that is needed to achieve high data rates. Both the orthogonal frequency division multiplexing (OFDM), and the single carrier with frequency domain equalization (SC-FDE) require accurate and reliable estimates of the channel transfer function (CTF) that can be obtained using known pilot-symbols at the price of a reduced spectral efficiency. The pilot-symbol aided CTF estimation (PACE) is important because it enables us to separate the estimation process from other physical layer functions such as the modulation and coding scheme (MCS) choice or resource allocation. A sophisticated pilot design should achieve a trade-off between the attainable accuracy of the channel estimate and

Received August 24, 2022 / Accepted October 07, 2022

Corresponding author: Veljko Stanković

University of Niš, Faculty of Electronic Engineering, Department of Telecommunications, Aleksandra Medvedeva 14,
18000 Niš, Republic of Serbia

E-mail: veljkost@gmail.com

the bandwidth efficiency in terms of the pilot overhead. These requirements are achieved in certain scenarios by using a scattered pilot grid, where pilot symbols are equidistantly spaced in time and frequency. It facilitates a flexible and adaptive air interface pilot aided channel estimation.

Pilot symbols are scattered in time and frequency such that the Nyquist sampling criterion is satisfied. The interpolation over pilot symbols suffers from the edge effect, where the estimation error significantly increases near the edges of a sequence to be estimated. It is particularly the case near the beginning and at the end of a frame in time, as well as for the subcarriers at the edges of the frequency bandwidth. An estimate of CTF for data subcarriers is obtained by the interpolation between pilot symbols.

The optimum solution for PACE is given by the Wiener interpolation filter [1], [2]. However, an optimum Wiener interpolation filter may be too complex for a practical implementation, because of large dimensions, and the requirement of the channel statistics knowledge. The computation of the filter coefficients in real time has a significant computational load. The computational complexity of the optimum Wiener interpolation filter can be reduced by reducing the dimension and by matching the model to a typical worst case scenario, so the filter coefficients can be precomputed and stored, [3]. A CTF interpolation that is based on the discrete Fourier transform (DFT) is computationally more efficient [4]. The DFT interpolation can be performed very efficiently by two successive DFTs and zero padding. In this case, we rely on the fact that the channel impulse response (CIR) in the time domain is time limited, and that the CIR components are mutually uncorrelated. Unfortunately, since the relative time delay between the CIR components is an exponential random variable, and CIR components are not equally spaced, after DFT of the frequency domain samples, there will be a leakage, and aliasing between the CIR components. The aliasing between the CIR components results in a mean-squared-error (MSE) floor that is much higher than that for the Wiener interpolation. The DFT interpolation MSE error floor is reduced by additional processing using the window function in the frequency domain, and by placing pilot symbols at the first, and at the last subcarrier. Additionally, in [1] the authors use the Wiener filtering in the time domain to reduce the aliasing, which unfortunately requires the knowledge of the CIR statistics, and assumes unrealistically that the CIR components are equally spaced. The same model mismatch is used in [5] to improve the performance of the DFT interpolation, and reduce the edge MSE by extrapolating the pilot tones into the guard bands by using the Wiener filter. Model mismatch assumes a worst case uniform power delay profile with maximum time delay spread. The estimator in [5] significantly reduces the MSE error floor, and at medium signal-to-noise ratios (SNRs) achieves the same performance as the optimum Wiener interpolation filter. Recently, there have been several proposals to use deep neural networks for the CTF estimation. In [12], the time-frequency grid of the channel response is modeled as a two-dimensional image which is known only at the pilot positions. This channel grid with several pilots is considered as a low-resolution image and the estimated channel as a high-resolution one. In the first step, an image super-resolution algorithm is used to enhance the resolution of the low-resolution input. Secondly, an image restoration method is utilized to remove the noise effects. The resulting algorithm does not achieve the MSE of the Wiener interpolation filter, and its performance is highly dependent on SNR at which the neural network is trained.

The CTF estimation error can be separated into two components [6]. The first component depends on the additive noise, and it dominates at low SNRs. As SNR increases, the CTF estimation error linearly reduces. The interpolation error, on the other hand, is independent of

SNR. At high SNRs, the CTF estimation error is dominated by the interpolation error that results in the MSE floor. Unfortunately, both the additive noise, and interpolation error are dependent on the subcarrier index. In particular, near the beginning and at the end of the sequence edge effects result in an increased estimation error.

In this paper we will introduce the DFT based interpolation, that does not rely on the mismatch model, and does not use computationally more demanding Wiener filtering. We rely on the characteristics of the process of the CTF bandlimiting, and sampled signal characteristics in time, and frequency domain in order to significantly reduce or even eliminate the edge effect, and consequently the MSE floor, by using the appropriate window functions (WF) in time, and frequency domain. Our goal is to achieve the estimation performance that is the same or close to the Wiener interpolation filter, with the computational complexity that is same or comparable to the DFT interpolation, and without any mismatch or channel statistics assumptions.

This paper is organized as follows. In Section 2, the system model is described. The CTF interpolation algorithm is presented in Section 3. In Section 4 we present the numerical results, and in Section 5 we give our conclusions.

2. SYSTEM MODEL

Consider an OFDM system where symbols are generated by using an N -point DFT, with N_c subcarriers that are used for the transmission, and N_g subcarriers in the guard bands at the signal bandwidth edges. Assuming perfect timing and frequency offset synchronization, the received signal of subcarrier n of the OFDM symbol is given by:

$$y_n = h_{f,n} x_n + v_n, \quad (1)$$

where $0 \leq n \leq N - 1$, x_n is the symbol transmitted on the n -th subcarrier, v_n is the sample of the additive white Gaussian noise on the n -th subcarrier. We assume that v_n are zero mean, complex Gaussian random variables with variance σ_v^2 . If we assume that the CIR has K components, with exponential power delay profile, then

$$h_{f,n} = \sum_{k=1}^{N_{cir}} h_k e^{-j \frac{2\pi}{N} n \tau_k}, \quad (2)$$

where h_k is the k -th CIR component, with time delay τ_k that is normalized to the sampling time T_0/N . OFDM symbol duration is denoted as T_0 .

We assume that the first, and the last N_g subcarriers are in the guard band, and that the maximum time delay spread $\tau_{N_{cir}}$ is less than or equal to the OFDM cyclic prefix with N_{cp} samples. In order to satisfy the Nyquist sampling criterion, the number of the pilot subcarriers N_p should be at least $2N_{cp}$, [6]. Spacing between the pilot symbols is equal to N/N_p . We assume that the first, and the last subcarrier are known pilot symbols.

3. TIME-FREQUENCY WINDOWED DFT INTERPOLATION

By taking the N -point DFT of the sequence that is given in (2), we obtain the time domain samples of the CIR as:

$$h_{f,m} = \frac{1}{\sqrt{N}} \sum_{n=0}^{N-1} h_{f,n} e^{j\frac{2\pi}{N}nm}, \quad (3)$$

which can be shown from (2) to be equal to:

$$h_{f,m} = \frac{1}{\sqrt{N}} \sum_{k=1}^{N_{cir}} h_k \sum_{n=0}^{N-1} e^{-j\frac{2\pi}{N}n(\tau_k-m)}, \quad (4)$$

which actually represents the sampled sequence of the convolution between the CIR, and a function:

$$\frac{1}{\sqrt{N}} \sum_{n=0}^{N-1} e^{-j\frac{2\pi}{N}n(\tau_k-m)} = \frac{1}{\sqrt{N}} \frac{1 - e^{-j2\pi(\tau_k-m)}}{1 - e^{-j\frac{2\pi}{N}(\tau_k-m)}}, \quad (5)$$

that is infinite, and results in component aliasing. By taking N samples of the CTF we have introduced a limit to the time domain estimation resolution, and performed a circular expansion of the CTF in the frequency domain, and of the CIR in the time domain. The edge effect is the result of our attempt to estimate samples of aperiodic functions, based on their circular expansions. In order to reduce the edge effect, and the MSE floor we need to eliminate or reduce the effects of the circular expansion of the CTF, and the CIR.

We will achieve this by taking several steps before interpolation. In the frequency domain we will use a flat-top WF to select the N -sample signal, and the edge subcarriers will no longer sharply change, but gradually go to zero. Next, we will add a sequence of N zeros in order to reduce aliasing in the frequency domain the will result from the processing in the time domain. Since our aim is not to estimate the exact values of the CIR components h_k , and their corresponding delays τ_k , before DFT we will multiply the sequence $h_{f,n}$ with the WF that should have such properties to reduce the time domain aliasing as much as possible. That is, WF should provide as low as possible the peak side-lobe level (PSL) relative to the main-lobe, and the asymptotic side-lobe attenuation (ASA). However, after the interpolation we will need to remove the effect of this WF, and therefore at the edges the value of this WF should be greater than zero in order to avoid significant noise amplification. This limits the ASA of WF to -6 dB/oct. This approach has already been proposed in the literature, but with different optimization parameters of WF, [5], [7], whereas in [1], anti-aliasing is performed directly, and only in the time domain. After we transform the signal to the time domain, we will first find the minimum point of the CIR aliasing due to its circular expansion, and smooth the transition between the circularly expanded parts of CIR in order to reduce the aliasing, and the estimation error in the frequency domain after the interpolation. The per-processing in the frequency domain is shown in Fig. 1, and the time domain processing in Fig. 2.

Signal selection WF, $w_{sel}(n)$ is equal to one for $n = N_{ws}, \dots, N - N_{ws} - 1$, and for $n = 0, \dots, N_{ws} - 1$, and $n = N - N_{ws}, \dots, N - 1$ it is equal to $w_o(n)$ that has desirable PSL, and ASA. From Fig.1 we can see that N_{ws} can be chosen to be greater than the guard band width in order to achieve better spectral properties. The rationale is that this part of the frequency domain sequence is the one that is most affected by the edge effect, and that therefore some

attenuation is acceptable if we can achieve lower estimation MSE. In general, we choose $w_d(n)$ such that for $n > N_g$, the subcarrier attenuation is not greater than 2dB. After interpolation, we will have some values for subcarriers in the guard bands, but these values are in general discarded. After multiplying the CTF samples with the selection WF, we add a sequence of N zero samples. Zero padding of the sequence of CTF samples has two effects. First, we reduce the aliasing in the frequency domain that results from time domain processing, and circular expansion in the frequency domain. Second, by zero padding we double the sampling rate in the time domain. We could further increase the sampling rate, but it does not provide any additional gains, while it increases the computational load.

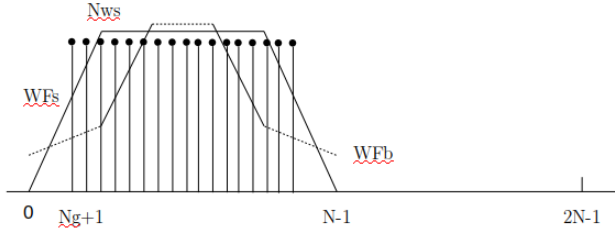


Fig. 1 Frequency domain signal selection using WF, and zero padding.

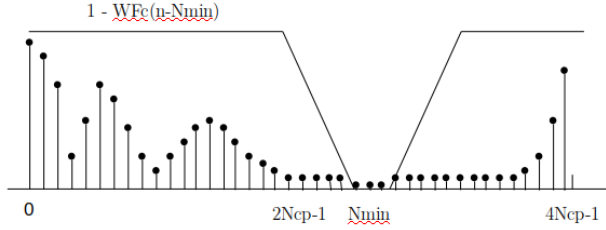


Fig. 2 Time domain signal spectral shaping using WF, and zero padding.

Let us denote a sequence of CTF samples on the pilot subcarriers as:

$$\mathbf{h}_{f,p} = \hat{\mathbf{h}}_{f, N_g + 1 + pN/N_p}, \quad (6)$$

$p = 0, \dots, N_p - 1$, where

$$\hat{\mathbf{h}}_{f,n} = h_{f,n} w_b(n), \quad (7)$$

are the filtered CTF samples using the second type of WF that is characterized by low spectral leakage, and minimum aliasing in time domain. Sample parameters are chosen such that the first and the last subcarrier are pilot subcarriers. If we introduce the following vectors of CTF samples:

$$\mathbf{h}_f = [h_{f,0} \cdots h_{f,N-1}]^T, \quad (8)$$

The vector of WF that is used for the time domain spectral shaping:

$$\mathbf{w}_b = [w_{b,0} \cdots w_{b,N-1}]^T, \quad (9)$$

we can write:

$$\hat{\mathbf{h}}_f = [\mathbf{h}_f \otimes \mathbf{w}_b; \mathbf{0}_N] \in \mathbb{C}^{2N \times 1}, \quad (10)$$

where \otimes denotes the Haddamard matrix product. Let us denote a vector of CTF samples only on the pilot subcarriers of $\hat{\mathbf{h}}_f$ as $\hat{\mathbf{h}}_{f,p}$, then we can write that:

$$\hat{\mathbf{h}}_{t,p} = \mathbf{F}_{2N_p}^H \hat{\mathbf{h}}_{f,p}, \quad (11)$$

where $\hat{\mathbf{h}}_{t,p}$ denotes the vector of CIR samples in the time domain of size $2N_p \times 1$. The $2N_p$ -point DFT matrix is denoted as \mathbf{F}_{2N_p} .

Next, we search for the point in the second half of the vector $\hat{\mathbf{h}}_{t,p}$ that has minimum envelope, and expand the length of the pilot CIR to $2N$:

$$N_{\min} = \min \hat{\mathbf{h}}_{t,p}(N_p : 2N_p), \quad (12)$$

where $\mathbf{a}(i:j)$ denotes the range of elements of a vector that are used for optimization. Spectral shaping in the frequency domain is performed by:

$$\tilde{\mathbf{h}}_{t,p} = \hat{\mathbf{h}}_{t,p} \otimes (1 - \mathbf{w}_c(\gg N_{\min})), \quad (13)$$

where WF $\mathbf{w}_c(\gg N_{\min})$ denotes WF \mathbf{w}_c that is shifted to the right by N_{\min} samples. Choice of \mathbf{w}_c will influence interpolation of the CTF samples between the pilot CTF samples, and the spectral leakage in the frequency domain. Finally, at N_{\min} position of $\tilde{\mathbf{h}}_{t,p}$ we add $2N - 2N_p$ zeros:

$$\bar{\mathbf{h}}_t = [\tilde{\mathbf{h}}_{t,p}(1:N_{\min}); \mathbf{0}_{2(N-N_p)}; \tilde{\mathbf{h}}_{t,p}(N_{\min}+1:2N_p)], \quad (14)$$

where $\mathbf{0}_M$ denotes all zero element vector of size $M \times 1$.

Finally, we interpolate CTF by taking DFT:

$$\bar{\mathbf{h}}_f = \mathbf{F}_{2N} \bar{\mathbf{h}}_t, \quad (15)$$

and by taking only the first N samples, and compensate for the time domain spectral shaping WF \mathbf{w}_b , we obtain the interpolated CTF:

$$\tilde{\mathbf{h}}_f = \bar{\mathbf{h}}_f(1:N) \otimes \mathbf{w}_b^{-1}. \quad (16)$$

The proposed time-frequency spectral shaping DFT interpolation has a slightly higher computational load in comparison to the regular DFT interpolation, because it requires two DFT operations at two times more points, $2N_p$, and $2N$, and one additional vector multiplication with the selection WF.

4. NUMERICAL RESULTS

Performance of the DFT interpolation with time-frequency spectral shaping will depend on the choice of the parameters of WFs that are used for specific goals. In order to be flexible, and able to fine tune specific parameters of each WF that is used, we will use the adjustable WF that provide us with the possibility to choose all the parameters that influence resolution, and spectral leakage, [8]. The adjustable WFs that are proposed

in [9] are based on ultraspherical polynomials, and also allow us to adjust the WF parameters depending on the required spectral properties. However, it has been shown that WFs proposed in [8] result in lower main-lobe width, because side-lobes near the main-lobe have in some parts constant amplitude. The Dolph-Chebyshev WF does have the lowest main lobe width. However, the first and the last sample of its impulse response are much higher, which results in undesirable response averaging, and it is therefore rarely used in practice, [8].

All of the WFs that are used in this paper are obtained iteratively as [8]:

$$w_m(n) = \beta_m w_{m-1}(n) + (1 - \beta_m) w_H^{\alpha+m+\Delta_m}(n), \quad (17)$$

where $n = 0, \dots, N_w - 1$, N_w , is the length of the WF, and the real valued parameters $\alpha \geq 0$, $0 \leq \beta_m \leq 1$, Δ_m , and $\Delta_0 = 0$ control the spectral properties of the WF. WF $w_H(n)$ denotes the Hann WF:

$$w_0(n) = w_H(n) = \left(\frac{\pi}{N_w} n \right)^2. \quad (18)$$

In our simulations we will use WFs with the following parameters:

- 1) \mathbf{w}_a : $m = 1$, $\alpha = 0.34$, $\beta_1 = 1$, $\Delta_1 = 1$, $N_w = 38$,
- 2) \mathbf{w}_b : $m = 3$, $\alpha = 0$, $\beta = [0.26 \ 0.221 \ 0.742]$, $\Delta = [0.818 \ 0.072 \ 0.92]$, $N_w = N$,
- 3) \mathbf{w}_c : $m = 1$, $\alpha = 0.34$, $\beta_1 = 1$, $\Delta_1 = 1$, $N_w = 9$,

Chosen WFs have the following spectral properties. WF that is used to select signal in the frequency domain \mathbf{w}_a , has PSL of -20dB, ASA of -10dB/oct, and variable window length of $N_w / 2 = 19$. WF that is used for spectral shaping in the time domain \mathbf{w}_b , has PSL of -20dB, and ASA of -6dB/oct, while its window length will vary depending on the specific length of the sequence in the frequency domain. The last WF \mathbf{w}_c , that is used for spectral shaping in the frequency domain has also PSL of -20dB, ASA of -10dB/oct, and the window length of $N_w = 9$.

The parameters of \mathbf{w}_a are chosen so that in our simulations it does not span more than three pilot subcarriers on each side of the signal bandwidth, and that the maximum attenuation in this range does not exceed more than 2dB. These subcarriers are only a couple of percents of the total number of subcarriers, and by shaping this part of the useful spectrum helps us reduce the edge MSE on one hand, with the acceptable loss that can be compensated by using the forward error correction coding over all subcarriers, including the majority that will have much lower CTF estimation error. Parameters of the second WF, \mathbf{w}_b , are chosen such to have the spectral leakage as low as possible. We gave priority to minimizing the PSL because we needed to minimize the aliasing between the neighboring CIR components, especially the first, and the last one. By padding the sequence in the frequency domain with N zeros, we are more flexible with the choice of the WF \mathbf{w}_c . Its parameters are chosen as a compromise between the minimum main-lobe width, and the ASA. These two parameters are inversely proportional, and as ASA decreases, resulting in lower spectral leakage, the main-lobe width increases, which results in lower frequency resolution. The main lobe of the chosen WF is only slightly greater than the main-lobe width of the rectangular WF, but has lower ASA by -4dB/oct that is enough considering the number of padded zeros in the frequency domain. We note that in a conventional DFT interpolation, the time domain processing is performed by using rectangular WF \mathbf{w}_c , which results in large spectral leakage at bandwidth edges.

In our simulations we have set that the cyclic prefix (CP) of the OFDM symbol is $N_{cp} = 16$. In order to satisfy the Nyquist sampling criterion, we set $N_p = 32$. First, we will compare the performance of the conventional DFT interpolation, and the proposed time-frequency DFT interpolation for $N = 320$. In case of conventional DFT we set that $N_{min} = N_p / 2$, and that no WF are used. Next, for comparison we use the case of the conventional DFT when we use the same WF to select the signal in the frequency domain as in the case of our proposed algorithm. This algorithm is denoted as conWDFT.

CIR is modeled with exponential power delay profile. Number of CIR components has the Poisson distribution, and the time delay between the CIR components is exponentially distributed, [10], [11]. Maximum power attenuation is set to -25 dB. CIR is normalized so that the average power of the CTF sample is equal to one. SNR is defined as the ratio of the average CTF sample power, and additive noise variance.

In Fig. 3, we compare three algorithms for CTF interpolation when the maximum time delay of the CIR is equal to the CP time interval. Simple frequency domain shaping of the bandwidth edges provides addition 5 dB MSE reduction with respect to the conventional DFT. The proposed spectral shaping using WFs in both time, and frequency domain provides more than 12 dB gain over the conventional DFT interpolation.

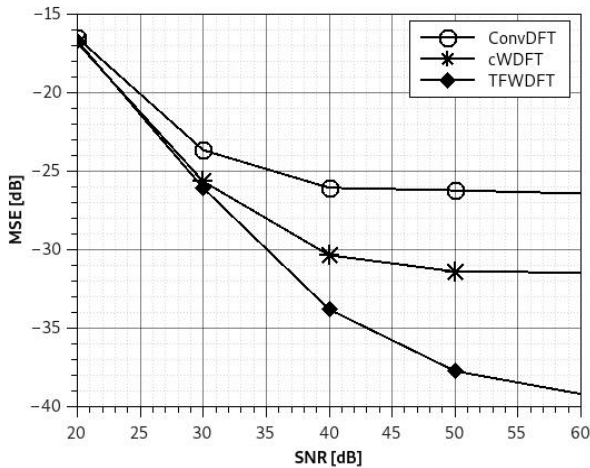


Fig. 3 MSE comparison for $T_m = T_{cp}$.

Case when the channel time delay spread is equal to CP is a worst case scenario. Very often it is much shorter than CP. In Fig. 4, we compare the same algorithms when the channel time delay spread is 80%, 60%, and 40% of CP, $T_m = 0.8 T_{cp}$, $T_m = 0.6 T_{cp}$, and $T_m = 0.4 T_{cp}$.

In this case, the DFT interpolation with frequency domain shaping has 7 dB gain over the conventional DFT interpolation, whose performance has not changed.

Finally, in Fig. 5, we compare MSE of the various algorithms as a function of the number of samples in the frequency domain for $SNR = -80$ dB, and $T_m = 0.6 T_{cp}$. As this number decreases, and with all other parameters fixed, the result is that the number of subcarriers between the pilot subcarriers also reduces. This has an effect only on the conventional DFT with the frequency domain WF selection, MSE significantly reduces. Performance

of the conventional DFT interpolation does not change with the time delay spread of CIR, or the spacing between the pilot subcarriers.

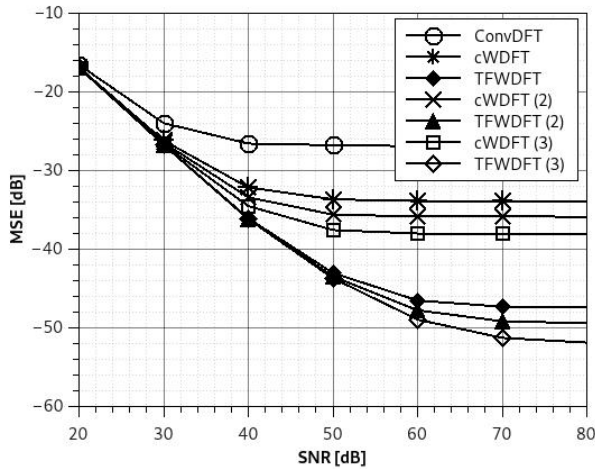


Fig. 4 MSE comparison for $T_m = 0.8T_{cp}$, (2) $T_m = 0.6T_{cp}$, and (3) $T_m = 0.4T_{cp}$.

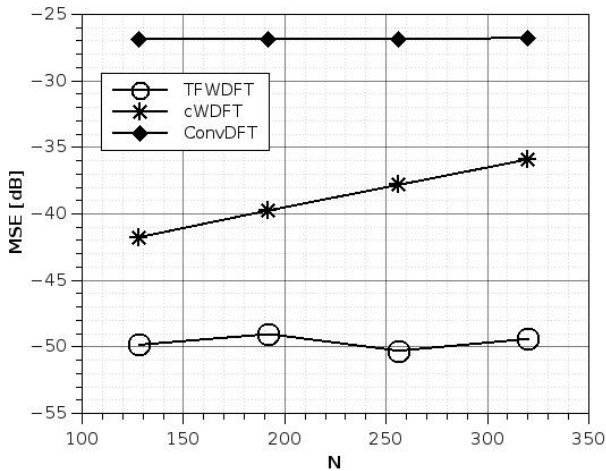


Fig. 5 MSE as a function of N , SNR = -80dB.

The algorithm that is proposed in this paper does not eliminate the edge effect. However, as a result of zero padding, and by using the first flat-top WF to select the sequence in the frequency domain, we significantly reduce the interpolation error, and the number of the subcarriers at the edges that are affected, in comparison to the conventional DFT interpolation or cWDFT. Overall, the interpolation error for TFWDFT in the middle of the bandwidth is significantly reduced to the point that at the high SNRs it is several orders of magnitude lower and almost negligible.

Computational complexity of the proposed algorithm TFWDFT, is two times higher than the complexity of cWDFT. However, it does achieve the MSE of the Wiener interpolation filter, and has a much lower MSE floor. However, its complexity is much lower than that of the Wiener interpolation filter which is a square function of the number of the subcarriers.

7. CONCLUSION

In this paper, we have introduced a novel low complexity channel estimation algorithm that is using DFT interpolation and the signal spectral shaping in time, and frequency domains in order to reduce the error floor that is characteristic for CTF estimation based on scattered pilot grid. We avoid using any worst case assumptions or Wiener filtering that requires the matrix inversion, and knowledge of the channel statistics. The spectral shaping is achieved using adaptive WFs that enable us to fine tune their parameters in order to meet a specific criterion. Depending on the length of CIR, the novel interpolation algorithm can achieve significant gains relative to other low complexity proposals.

Acknowledgement: *This work has been supported by the Ministry of Education, Science and Technological Development of the Republic of Serbia.*

REFERENCES

- [1] G. Auer, S. Sand, A. Dammann, "Comparison of Low Complexity OFDM Channel Estimation Techniques", In: *Proc. of Int. OFDM Workshop*. 2003.
- [2] G. Auer and E. Karipidis, "Pilot aided channel estimation for OFDM: a separated approach for smoothing and interpolation," in *Proc. IEEE ICC'2005*, vol. 4, pp. 2173-2178, May 2005. doi: 10.1109/ICC.2005.1494722
- [3] P. Hoehner, S. Kaiser, and P. Robertson, "Pilot-Symbol-Aided Channel Estimation in Time and Frequency," in *Proc. Communication Theory Mini-Conf. (CTMC) within IEEE Global Telecommun. Conf. (GLOBECOM'97)*, Phoenix, USA, pp. 90–96, 1997. doi: 10.1007/978-1-4615-6231-3_20
- [4] B. Yang, Z. Cao, and K. B. Letaief, "Analysis of low-complexity windowed DFT-based MMSE channel estimator for OFDM systems," *IEEE Trans. Commun.*, vol. 49, no. 11, pp. 1977-1987, Nov. 2001. doi: 10.1109/26.966074
- [5] J.W. Seo et al., "An enhanced DFT-based channel estimation using virtual interpolation with guard bands prediction for OFDM", in *Proc.PIMRS06*, 2006. doi: 10.1109/PIMRC.2006.254263
- [6] D2.1 Identification of Radio-link technologies, Technical report, IST-2003-507581 WINNER
- [7] AJ van-der Veen, M.C. Vanderveen, A. Paulraj, "Joint angle and delay estimation using shift-invariance techniques", *IEEE Trans. on Sig. Proc.*, vol.46, No 2, February 1998. doi: 10.1109/78.655425
- [8] V. Stankovic, "Adjustable high resolution window function", *El. Lett.*, vol 54, No 13, p. 827-829, June 2018. DOI: 10.1049/el.2018.0448
- [9] S.W.A Bergen, A. Antoniou: 'Design of ultraspherical window functions with prescribed spectral characteristics', *EURASIP J. Appl. Signal Process.*, vol 2004, No 1, pp. 2053–2064, 2004 doi: 10.1155/S1110865704403114
- [10] A. A. M. Saleh and R. A. Valenzuela, "A statistical model for indoor multipath propagation," *IEEE J. Sel. Areas Commun.*, vol. SAC-5, pp.128–137, Feb. 1987. doi: 10.1109/JSAC.1987.1146527
- [11] Meijerink, A., & Molisch, A. F. (2014). On the physical interpretation of the Saleh–Valenzuela model and the definition of its power delay profiles. *IEEE Transactions on Antennas and Propagation*, 62(9), 4780-4793. doi: 10.1109/TAP.2014.2335812
- [12] S. Mehran, et al. "Deep learning-based channel estimation." *IEEE Communications Letters* vol 23, No. 4, p. 652-655. April 2019. doi: 10.1109/LCOMM.2019.2898944

PERFORMANCE OF SECURE COMMUNICATION OVER α -FISHER-SNEDECOR FADING CHANNELS

UDC (621.395.38+629.783)

**Jelena Anastasov, Aleksandra Panajotović,
Dejan Milić, Daniela Milović**

University of Niš, Faculty of Electronic Engineering, Department of Telecommunications,
Republic of Serbia

Abstract. *In this paper, we investigate the physical layer security (PLS) of the traditional Wyner's wiretap channel model. Secrecy performance analysis is performed assuming a presence of an active eavesdropper trying to overhear the confidential data transmission from the source node to the predefined destination. In what follows, we derive the lower bound of the secrecy outage probability, the strictly positive secrecy capacity as well as the average secrecy capacity, over the composite α -Fisher-Snedecor (α -F) fading environment. According to the analytical results, numerical results are also shown. The impact of the path loss component, the average signal-to-noise ratios over the main/wiretap channel as well as the impact of the fading, the non-linearity of the propagation medium and the shadowing shaping parameter on the PLS metrics is examined. The overall analysis and the obtained results have a high level of generality and also a high level of applicability since the α -F distribution was recently proposed, as the best fit distribution for the channel characterization of the device-to-device wireless communication in the future Beyond 5G networks.*

Key words: *Composite fading channel, physical layer security, device-to-device communication*

1. INTRODUCTION

The amount of wirelessly transmitted data constantly increases with rapid development of new emerging concepts and technologies such as the Internet-of-Things (IoT) and 6G [1]. Due to the open access property in wireless communications, it is of high significance to provide a secure data transmission, especially for private and sensitive data.

Received August 30, 2022 / Accepted September 27, 2022

Corresponding author: Jelena Anastasov

University of Niš, Faculty of Electronic Engineering, Department of Telecommunications, Aleksandra Medvedeva 14, 18000 Niš, Republic of Serbia

E-mail: jelena.anastasov@elfak.ni.ac.rs

Cryptography, as a built-in technique at system's upper layers, can be used to achieve this goal [2]. Cryptographic protocols promote a shared-key concept between authorized entities, which can be inconvenient in networks with massive number of devices. In addition, the eavesdroppers, as authorized or unauthorized users, usually own unlimited computing power and can easily break down confidential keys by utilizing the brute force attack method. This is why the cryptography requires to be strengthened.

The information-theoretic security has gained increased attention over the recent years by imposing the concept of secure data transmission on the physical layer [3]. The physical layer security (PLS) approach addresses the security issue by exploiting the dynamic characteristics of the propagation channel which is prone to eavesdropping [4]-[6]. In [7], Wyner had introduced the notion of the wiretap channel between the source (Alice) and an eavesdropper (Eve), who tries to intercept the intended transmission to a legitimate receiver (Bob).

Numerous PLS works are established to develop high secrecy rates for classic Wyner's wiretap channel model [8]-[17]. In all of the existing researches, the security performance is analysed using several metrics in the context of different wireless communication systems and over various fading channels. In what follows, a detailed PLS literature overview for basic wiretapped system model over fading channels, is given.

The strictly positive secrecy capacity (SPCS) has been determined in [8] over large open area with a line-of-sight between the transmitter and the receiver. The secure transmission between two nodes over α - μ fading channels, which include the non-linearity of propagation media, is analysed in [9], in terms of the average secrecy capacity (ASC). Novel analytical expressions for the SPSC and a lower bound on the secrecy outage probability (SOP) are derived over κ - μ fading channels, in [10], and further applied to performance studies of different emerging wireless applications, such as cellular device-to-device (D2D), vehicle-to-vehicle, peer-to-peer, and body centric communications. In addition, the expressions for the SPSC and a lower bound on SOP over a mixture of α - μ / κ - μ , and vice versa, fading channels are derived in [11].

The secrecy capacity for classic Wyner's wiretap model over a non-small scale fading channels, i.e. over the independent/correlated lognormal fading channels is investigated in [12]. A detailed analysis of all PLS metrics, that encompasses the interplay of both the fading and the shadowing phenomenon, over generalized- K fading channels, is given in [13], [14]. In [15], the SOP and the SPSC are analysed over shadowed κ - μ fading environment, with the aid of the moment matching method.

The Fisher-Snedecor (F) distribution was proposed in [16] to characterize the composite fading conditions over D2D communication channels at 5.8GHz, as less simple than the generalized- K . The SOP, the SPSC, the ASC and asymptotic ASC over F fading channels are investigated in [17], [18].

Recently, the author in [19] has proposed an even more general composite fading distribution, the α -Fisher-Snedecor (α - F) fading distribution that characterize, the nonlinearity of the propagation media, in addition to the fading and shadowing phenomena in the wireless channel. This model is pronounced as the best fit for the realistic channel measurements for D2D communications and underwater acoustic. To the best of authors' knowledge the PLS analysis over α - F fading has not yet been reported.

In this paper, we present the detailed PLS analysis of the basic wiretap model over α - F fading channels. Novel expressions for evaluating the asymptotic ASC, lower bound on the SOP and the exact SPSC are derived. These expressions are quite general and can be

simplified to Gamma, Weibull, Nakagami- m , exponential, α - μ , one-sided Gaussian and F fading scenarios. The interplay of various channels' parameters as well as the average SNRs over main/wiretap channel on the PLS is analysed.

The main contributions of this work can be summarized as:

- novel analytical forms of PLS metrics for source-destination-eavesdropper communication model, over general α - F fading channels, are given
- impact of the interplay of the fading depth, shadowing severity and nonlinearity parameter of the main/wiretap channel on secure transmission between the source and intended node, is examined
- in addition, the path loss component is taken into analysis
- presented results of α - F fading model can accommodate other existing fading scenarios, based on the estimate of α - F distribution parameters

The list of parameters, symbols and abbreviations throughout the paper is given in Table 1, to make easier for the reader to follow.

Table 1 List of notations, symbols, abbreviations

Notations, symbols, abbreviations	
*	designates: M for the main channel, E for the wiretap (eavesdropper's) channel
h_*	channel fading coefficient
γ_*	instantaneous signal-to-noise ratio (SNR)
d_*	distance from the source to the destination/eavesdropper
ξ	path loss parameter
m_{s_s}	shadowing severity factor
α_*	nonlinearity propagation factor
μ_*	fading depth parameter
$\bar{\gamma}_*$	average SNR
C_s	secrecy capacity
\bar{C}_s	average secrecy capacity (ASC)
ρ	average main-to-eavesdropper's channel power ratio (MER)
P_{out}^{EX}	exact secrecy outage probability (SOP)
P_{out}^L	lower bound of SOP
P_{nz}	strictly positive secrecy capacity (SPSC)
r	ratio between the main and wiretap link distances
$G_{p,q}^{m,n}(\cdot)$	univariate Meijer's G function
$H_{p,q}^{m,n}(\cdot)$	Fox's H function

2. PROBLEM FORMULATION

The system model we used in the analysis is shown in Fig.1. The source transmits the secret message by emitting signal $s(t)$, with $E[|s(t)|^2] = 1$, and therefore the signal received by the destination can be written in the following way

$$x_M(t) = \sqrt{P}h_M s(t) + n_M(t), \quad (1)$$

where P denotes the emitting power from the source, h_M represents a fading coefficient of the main channel i.e. the channel between the source and destination, and $n_M(t)$ denotes the additive white Gaussian noise (AWGN). The destination node is at the distance d_M from the source. The illegitimate node is also in the area of coverage, at the distance d_E from the source. The intruder tries to overhear the desired signal, and thus the receiving signal at the eavesdropper can be defined as

$$x_E(t) = \sqrt{P}h_E s(t) + n_E(t), \quad (2)$$

where h_E denotes a fading coefficient of the wiretap channel i.e. the channel between the source and eavesdropper, and $n_E(t)$ denotes the AWGN. The channel state information (CSI) of both channels is available at the source [3].

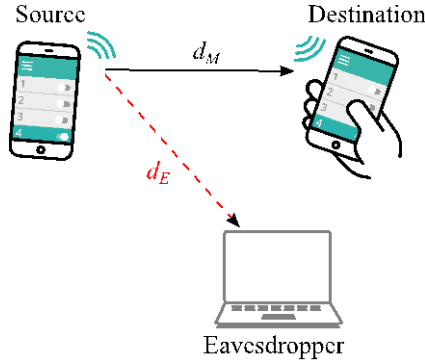


Fig. 1 System model

Let us express the instantaneous signal-to-noise-ratios (SNRs) over the main or wiretap link as

$$\gamma_* = \frac{|h_*|^2 P}{\sigma_*^2 d_*^\xi}, \quad (3)$$

where the subscript, *, denotes either main (M), either eavesdropper's (E) channel index, σ_*^2 defines a variance of zero-mean AWGN and d_* denotes the distance between two nodes, while parameter ξ characterizes the path loss.

Following the assumption that the main and wiretap channel are corrupted by α -F fading, the probability density function (PDF) of the instantaneous SNR, over both channels, has the form [19]

$$p_{\gamma_s}(\gamma) = \frac{\alpha_*}{2B(\mu_*, m_{s_*})} \left(\frac{(m_{s_*} - 1)\bar{\gamma}_*^{\frac{\alpha_*}{2}}}{\mu_* \lambda_*^{\frac{\alpha_*}{2}} d_*^\xi} \right)^{m_{s_*}} \gamma^{\frac{\alpha_* \mu_*}{2} - 1} \times \left(\gamma^{\frac{\alpha_*}{2}} + \frac{(m_{s_*} - 1)\bar{\gamma}_*^{\frac{\alpha_*}{2}}}{\mu_* \lambda_*^{\frac{\alpha_*}{2}} d_*^\xi} \right)^{-(\mu_* + m_{s_*})}, \quad (4)$$

where $B(\cdot, \cdot)$ denotes the Beta function [20], $\bar{\gamma}_*$ is the average SNR; m_{s_*} is the shadowing severity parameter, $m_{s_*} > 1$, μ_* is the fading depth parameter, $\mu_* \geq 0.5$, α_* is the non-linearity of the propagation medium, $\alpha_* > 0$, and λ_* is the parameter defined as

$$\lambda_* = \left(\frac{m_{s_*} - 1}{\mu_*} \right)^{\frac{2}{\alpha_*}} \frac{\Gamma\left(\mu_* + \frac{2}{\alpha_*}\right) \Gamma\left(m_{s_*} - \frac{2}{\alpha_*}\right)}{\Gamma(\mu_*) \Gamma(m_{s_*})}, \quad m_{s_*} > \frac{2}{\alpha_*}, \quad (5)$$

with $\Gamma(\cdot)$ being the Gamma function [20]. By utilizing the specific values of the Meijer's G function relying on [21, eq. (07.34.03.0271.01)] and the form of the argument simplification [21, eq. (07.34.16.0001.01)], the previous expression of the PDF can be rewritten as

$$p_{\gamma_s}(\gamma) = \frac{\alpha_*}{2\Gamma(\mu_*)\Gamma(m_{s_*})\gamma} G_{1,1}^{1,1} \left(\frac{\gamma^{\frac{\alpha_*}{2}}}{a_* \bar{\gamma}_*^{\frac{\alpha_*}{2}} / d_*^\xi} \middle| \begin{matrix} 1 - m_{s_*} \\ \mu_* \end{matrix} \right), \quad (6)$$

with $a_* = \frac{(m_{s_*} - 1)}{\mu_* \lambda_*^{\frac{\alpha_*}{2}}}$ and $G_{p,q}^{m,n}(\cdot)$ denoting the univariate Meijer's G function [20, Eq.

(9.301)]. The asymptotic PDF for the large average SNR values can be obtained with the help of [21, eq. (07.34.06.0001.01)], i.e. $\bar{\gamma}_* \rightarrow \infty$, and taking into account only the first term in summation, in the following form

$$p_{\gamma_s}^{asympt}(\gamma) = \frac{\alpha_*}{2B(\mu_*, m_{s_*})\gamma} \left(\frac{\gamma^{\frac{\alpha_*}{2}}}{a_* \bar{\gamma}_*^{\frac{\alpha_*}{2}} / d_*^\xi} \right)^{\mu_*}. \quad (7)$$

The cumulative distribution function (CDF) of the instantaneous SNR can be evaluated, relying on [22, Eq. (26)], as

$$F_{\gamma_s}(\gamma) = \frac{1}{\Gamma(\mu_*)\Gamma(m_{s_*})} G_{2,2}^{1,2} \left(\frac{\gamma^{\frac{\alpha_*}{2}}}{a_* \bar{\gamma}_*^{\frac{\alpha_*}{2}} / d_*^\xi} \middle| \begin{matrix} 1 - m_{s_*}, 1 \\ \mu_*, 0 \end{matrix} \right). \quad (8)$$

In addition, the asymptotic CDF when $\bar{\gamma}_* \rightarrow \infty$ can be defined by recalling [21, eq. (07.34.06.0001.01)], as

$$F_{\gamma_*}^{asympt}(\gamma) = \frac{1}{B(\mu_*, m_{s_*})\mu_*} \left(\frac{\mu_*}{\alpha_* \bar{\gamma}_*^2 / d_*^\xi} \right)^{\mu_*} \gamma^{\frac{\alpha_* \mu_*}{2}}. \quad (9)$$

2. PHYSICAL LAYER SECURITY METRICS

In this Section, ASC, SOP and SPSC are analytically determined.

To evaluate the instantaneous channel capacity over the main channel as well as over the wiretap channel, we can rely on the Shannon capacity formula [3]

$$R_* = \log_2(1 + \gamma_*). \quad (10)$$

The first step to establish the ASC expression is to start from secrecy capacity as defined in [4]. The secrecy capacity is characterize as a difference between the channel capacities of the main and wiretap links, i.e. mathematically

$$C_s = R_M - R_E = \log_2 \left(\frac{1 + \gamma_M}{1 + \gamma_E} \right), \quad (11)$$

while assuming that the perfect CSIs are available at all nodes.

2.1. Analytical expression of ASC

ASC is frequently measured as a benchmark to indicate the average communication rate of the main transmission. The metric's definition can be given in the following form

$$\bar{C}_s = \iint_{\bar{D}} d\gamma_M d\gamma_E \log_2 \left(\frac{1 + \gamma_M}{1 + \gamma_E} \right) P_M(\gamma_M) P_E(\gamma_E); \quad \bar{D} = \begin{cases} 0 \leq \gamma_M < \infty \\ 0 \leq \gamma_E < \gamma_M \end{cases}. \quad (12)$$

The previous formula can be rewritten as

$$\begin{aligned} \bar{C}_s &= \int_0^\infty d\gamma_M P_M(\gamma_M) \int_0^{\gamma_M} \log_2 \left(\frac{1 + \gamma_M}{1 + \gamma_E} \right) P_E(\gamma_E) d\gamma_E, \\ &= I_1 + I_2 - I_3 \end{aligned} \quad (13)$$

where the integrals are defined as

$$I_1 = \int_0^\infty \log_2(1 + \gamma_M) P_M(\gamma_M) F_E(\gamma_M) d\gamma_M, \quad I_2 = \int_0^\infty \log_2(1 + \gamma_E) P_E(\gamma_E) F_M(\gamma_E) d\gamma_E \quad \text{and}$$

$I_3 = \int_0^\infty \log_2(1 + \gamma_E) P_E(\gamma_E) d\gamma_E$. To avoid solutions of the integrals in a form of complex bivariate Meijer's G functions, as it was done for the wiretap Fisher-Snedecor channel scenario in [18], we have determined the simplified form of ASC. Namely, the first and the second integral are asymptotically solved in the following forms

$$\begin{aligned}
I_1^{\text{asympt}} &= \frac{2^{\mu_M + m_{s_M} - 1} \mu_E^{\mu_E - 1}}{\ln(2)\Gamma(m_{s_M})\Gamma(\mu_M)(2\pi)^{\alpha_M} B(\mu_E, m_{s_E})} \left(\frac{\frac{\alpha_E}{\lambda_E^2}}{(m_{s_E} - 1)\bar{\gamma}_E^2 / d_E^\xi} \right)^{\mu_E} \\
&\times G_{2+2\alpha_M, 2+2\alpha_M}^{2+2\alpha_M, 2+2\alpha_M} \left(\left(\frac{\mu_M \lambda_M^2}{(m_{s_M} - 1)\bar{\gamma}_M^2 / d_M^\xi} \right)^2 \left| \begin{array}{l} \frac{1-m_{s_M}}{2}, \frac{2-m_{s_M}}{2}; \Delta\left(\alpha_M, -\frac{\alpha_E \mu_E}{2}\right); \Delta\left(\alpha_M, -\frac{\alpha_E \mu_E}{2}\right) \\ \frac{\mu_M}{2}, \frac{\mu_M + 1}{2}; \Delta\left(\alpha_M, -\frac{\alpha_E \mu_E}{2}\right); \Delta\left(\alpha_M, -\frac{\alpha_E \mu_E}{2}\right) \end{array} \right. \right) \quad (14)
\end{aligned}$$

and

$$\begin{aligned}
I_2^{\text{asympt}} &= \frac{2^{\mu_E + m_{s_E} - 1} \mu_M^{\mu_M - 1}}{\ln(2)\Gamma(m_{s_E})\Gamma(\mu_E)(2\pi)^{\alpha_E} B(\mu_M, m_{s_M})} \left(\frac{\frac{\alpha_M}{\lambda_M^2}}{(m_{s_M} - 1)\bar{\gamma}_M^2 / d_M^\xi} \right)^{\mu_M} \\
&\times G_{2+2\alpha_E, 2+2\alpha_E}^{2+2\alpha_E, 2+2\alpha_E} \left(\left(\frac{\mu_E \lambda_E^2}{(m_{s_E} - 1)\bar{\gamma}_E^2 / d_E^\xi} \right)^2 \left| \begin{array}{l} \frac{1-m_{s_E}}{2}, \frac{2-m_{s_E}}{2}; \Delta\left(\alpha_E, -\frac{\alpha_M \mu_M}{2}\right); \Delta\left(\alpha_E, 1 - \frac{\alpha_M \mu_M}{2}\right) \\ \frac{\mu_E}{2}, \frac{\mu_E + 1}{2}; \Delta\left(\alpha_E, -\frac{\alpha_M \mu_M}{2}\right); \Delta\left(\alpha_E, -\frac{\alpha_M \mu_M}{2}\right) \end{array} \right. \right), \quad (15)
\end{aligned}$$

where $\Delta(s, t) = \frac{t}{s}, \frac{t+1}{s}, \dots, \frac{t+s-1}{s}$ and when $\alpha_M, \alpha_E \in N^+$. The expressions (14) and (15) are obtained by substituting the asymptotic forms of CDFs in I_1 and I_2 , and then recalling [21, eq.(07.34.21.0011.01)]. The third integral is solved by substituting (6) into I_3 , and with the help of [23, eq. (2.24.1.1)] in the following way

$$\begin{aligned}
I_3 &= \frac{2^{\mu_E + m_{s_E} - 1}}{\ln(2)\Gamma(m_{s_E})\Gamma(\mu_E)(2\pi)^{\alpha_E}} \\
&\times G_{2+2\alpha_E, 2+2\alpha_E}^{2+2\alpha_E, 2+2\alpha_E} \left(\frac{\mu_E \lambda_E^2}{(m_{s_E} - 1)\bar{\gamma}_E^2 / d_E^\xi} \left| \begin{array}{l} \frac{1-m_{s_E}}{2}, \frac{2-m_{s_E}}{2}; 0, \dots, \frac{\alpha_E - 1}{\alpha_E}; \frac{1}{\alpha_E}, \dots, \frac{\alpha_E}{\alpha_E} \\ \frac{\mu_E}{2}, \frac{\mu_E + 1}{2}; 0, \dots, \frac{\alpha_E - 1}{\alpha_E}; 0, \dots, \frac{\alpha_E - 1}{\alpha_E} \end{array} \right. \right). \quad (16)
\end{aligned}$$

Thus, by summarizing (14), (15) and (16), the asymptotic ASC is determined.

2.2. Analytical expression of SOP

In the scenario with both the active/passive eavesdropping, SOP is very often measured to indicate conceptually the security of the authorized communication. From the information-theory point of view, SOP is a secrecy outage event when secrecy capacity falls below the target secrecy rate, R_t . Thus, SOP can be defined in the exact form, as [18]

$$P_{out}^{EX} = \Pr[C_s < R_t] = \Pr[\gamma_M \leq R_s \gamma_E + R_s - 1], \quad (17)$$

where $\gamma_0 = R_s \gamma_E + R_s - 1$ and $R_s = 2^{R_t}$. In the analysis that follows, we have determined the lower bounded version of SOP as [18]

$$\begin{aligned} P_{out}^L &= \Pr[\gamma_M \leq R_s \gamma_E] \leq P_{out} = \\ &= \int_0^\infty \int_0^{R_s \gamma_E} p_M(\gamma_M) p_E(\gamma_E) d\gamma_E d\gamma_M \\ &= \int_0^\infty F_M(R_s \gamma_E) p_E(\gamma_E) d\gamma_E. \end{aligned} \quad (18)$$

By substituting (8) and (6) with appropriate subscripts in (18), and with the help of [21, Eq. (07.34.21.0012.01)], by making the change of variables, $\gamma_E^{\alpha_E/2} = t$, the P_{out}^L integral is solved in the following form

$$\begin{aligned} P_{out}^L &= \frac{\alpha_M}{2\Gamma(m_{s_E})\Gamma(m_{s_M})\Gamma(\mu_E)\Gamma(\mu_M)} \\ &\times H_{3,3}^{2,3} \left(\begin{matrix} \frac{\alpha_M \alpha_E}{R_s^2} & a_E^{\alpha_M} r \\ a_M^{\alpha_E} \rho^{\frac{\alpha_M \alpha_E}{2}} \end{matrix} \middle| \begin{matrix} (1 - m_{s_M}, 1), (1, 1), \left(1 - \mu_E, \frac{\alpha_M}{\alpha_E}\right) \\ (\mu_M, 1), \left(1 + m_{s_E}, \frac{\alpha_M}{\alpha_E}\right), (0, 1) \end{matrix} \right), \end{aligned} \quad (19)$$

where $\rho = \bar{\gamma}_M / \bar{\gamma}_E$ defines the average main-to-eavesdropper's channel power ratio (MER), r denotes the ratio between the main and wiretap link distances, $r = d_M/d_E$, and $H_{p,q}^{m,n}(\cdot)$ is the notation of the Fox's H function [24, eq. (1.2)]. The Fox's H function is not commonly built-in function in *Mathematica* or *Matlab* software packages, but can be evaluated with the help of the program given in [25, Appendix]. Formula (19) can be rewritten in the simplified form of the Meijer's G function, when $\alpha_M, \alpha_E \in \mathbb{N}^+$, relying on [23, eq. (8.3.2.22)], in the following form

$$\begin{aligned} P_{out}^L &= \frac{\alpha_E^{\mu_M + m_{s_M} - 1} \alpha_M^{\mu_E + m_{s_E} - 1}}{(2\pi)^{\alpha_E + \alpha_M - 2} \Gamma(m_{s_E}) \Gamma(m_{s_M}) \Gamma(\mu_E) \Gamma(\mu_M)} \\ &\times G_{2\alpha_E + \alpha_M, 2\alpha_E + \alpha_M}^{\alpha_E + \alpha_M, 2\alpha_E + \alpha_M} \left(\begin{matrix} \frac{\alpha_M \alpha_E}{R_s^2} & a_E^{\alpha_M} r \\ a_M^{\alpha_E} \rho^{\frac{\alpha_M \alpha_E}{2}} \end{matrix} \middle| \begin{matrix} \Delta(\alpha_E, 1 - m_{s_M}), \Delta(\alpha_E, 1), \Delta(\alpha_M, 1 - \mu_E) \\ \Delta(\alpha_E, \mu_M), \Delta(\alpha_M, 1 - (1 - m_{s_E})), \Delta(\alpha_E, 0) \end{matrix} \right). \end{aligned} \quad (20)$$

2.3. Analytical expression of SPSC

The existence of non-zero secrecy capacity i.e. SPSC is assured with the probability given by

$$\begin{aligned} P_{nc} &= \Pr[\gamma_M > \gamma_E] = \\ &= \int_0^\infty F_E(\gamma_M) p_M(\gamma_M) d\gamma_M. \end{aligned} \quad (21)$$

Thus, by substituting (8) and (6) in (21) and once more recalling [21, eq. (07.34.21.0012.01)], we have derived SPSC in the following form

$$P_{nz} = \frac{\alpha_E}{2\Gamma(m_{s_E})\Gamma(m_{s_M})\Gamma(\mu_E)\Gamma(\mu_M)} \times H_{3,3}^{2,3} \left(\frac{\alpha_M \alpha_E \rho^2}{a_E^{\alpha_M} r} \left| \begin{array}{l} (1-m_{s_E}, 1), (1, 1), \left(1-\mu_M, \frac{\alpha_E}{\alpha_M}\right) \\ (\mu_E, 1), \left(1+m_{s_M}, \frac{\alpha_M}{\alpha_E}\right), (0, 1) \end{array} \right. \right). \quad (22)$$

By simplifying the Fox's H function with the help of [23, eq. (8.3.2.22)], SPSC is rewritten in the following form as

$$P_{nz} = \frac{\alpha_E}{2\Gamma(m_{s_E})\Gamma(m_{s_M})\Gamma(\mu_E)\Gamma(\mu_M)} \times G_{2\alpha_M+\alpha_E, 2\alpha_M+\alpha_E}^{\alpha_M+\alpha_E, 2\alpha_M+\alpha_E} \left(\frac{\alpha_M \alpha_E \rho^2}{a_E^{\alpha_M} r} \left| \begin{array}{l} \Delta(\alpha_M, 1-m_{s_E}), \Delta(\alpha_M, 1), \Delta(\alpha_E, 1-\mu_M) \\ \Delta(\alpha_M, \mu_E), \Delta(\alpha_E, 1-(1-m_{s_M})), \Delta(\alpha_M, 0) \end{array} \right. \right). \quad (23)$$

3. NUMERICAL RESULTS

In this section, numerical results of ASC, SOP and SPSC are presented to illustrate the carried out mathematical analysis. Numerical results are obtained using *Mathematica* and figures are drawn in *Origin* software package. In all figures, the path loss parameter is $\xi=2.7$, which is a commonly used value for the parameter that describes the path loss in a fading environment.

Fig. 2 illustrates ASC versus MER, ρ , for different space constellations of the destination and eavesdropper; and identically distributed (i.d.) fading links, $\alpha_M=\alpha_E=\alpha$, $m_{sM}=m_{sE}=m_s$, $\mu_M=\mu_E=\mu$. For higher values of the ratio r , i.e. when eavesdropper is closer to the source, the ASC values are lower, as expected. Also, as the fading depth, the nonlinearity as well as the shadowing severity over the propagation medium decreases (m_s , α and μ increase), ASC outperforms. In a more realistic scenario, when the destination is closer to the source in comparison to the eavesdropper's position ($r=0.8$), the most favorable channel conditions ($\alpha=3.4$, $m_s=4.8$, $\mu=3.8$) indicates lower or at least the same ASC values than less favorable channels case ($\alpha=2.4$, $m_s=3.8$, $\mu=2.8$). This i.d. channel feature can be utilized by the PLS approach in order to ensure a secure transmission. In this figure, the asymptotes are also obtained according to expressions (14), (15) and (16). The asymptotes show a good agreement with the exact results, especially for favorable channel conditions and favorable space constellation of nodes.

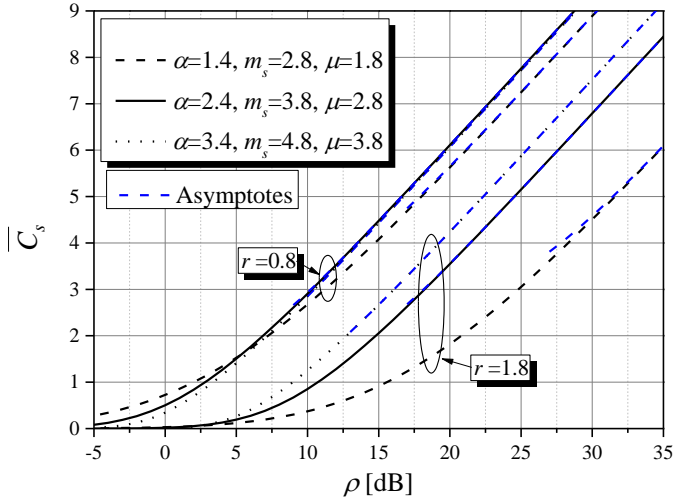


Fig. 2 The ASC vs. MER for different channel conditions and different distances of receiving nodes

SPSC in the function of the average SNR of the main channel for different average SNRs of the wiretap channel is shown in Fig. 3. One can notice that SPSC can be improved by assuring larger average SNR values of the main channels and/or lower average SNRs of the wiretap channel. The improvement is more obvious for higher nonlinearity parameter of the main channel, $\alpha_M = 5$, i.e. for lower nonlinearity of the main propagation medium.

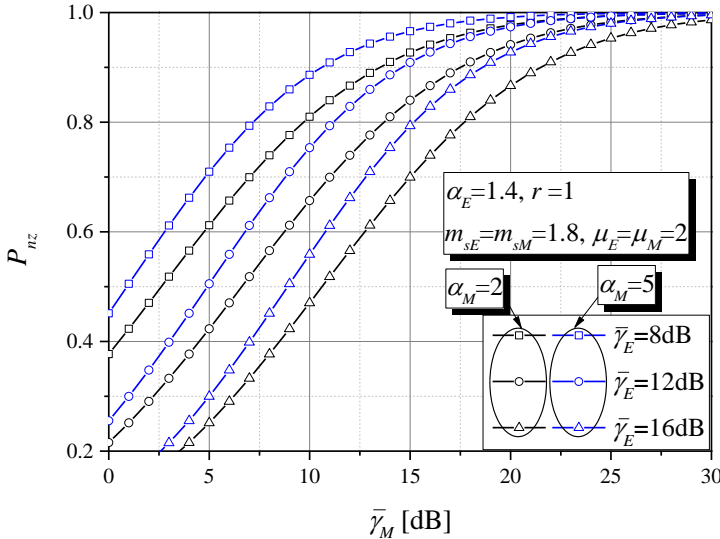


Fig. 3 SPSC vs. the average SNR values of the main channel for different nonlinearity propagation scenarios

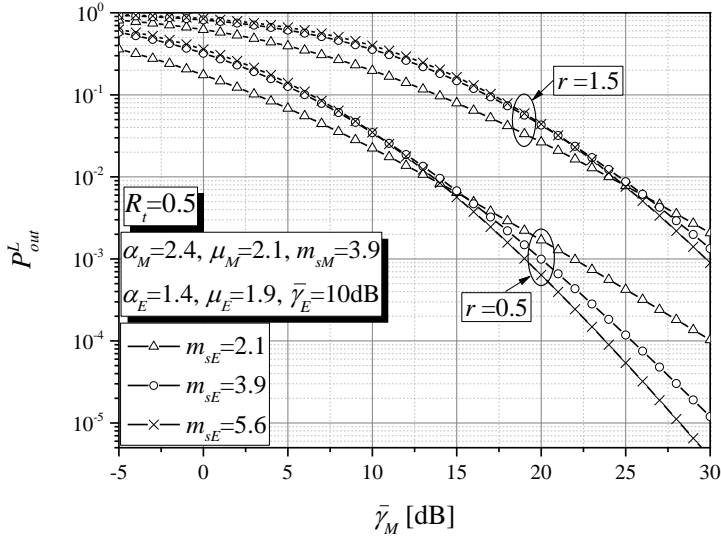


Fig. 4 Lower bound of SOP vs. the average SNR values of the main channel for different distances' ratios

The lower bound of SOP, versus the average SNRs of the main channel for different distance ratios and different fading depth scenarios over the wiretap channel, is demonstrated in Fig. 4. An interesting remark here is that up to some point the largest fading deepness over the wiretap channel assures the lowest SOP values, and then the interplay of the same fading parameter, m_{sE} , is vice versa. This is more obvious when the destination is closer to the source. For instance, when $r=0.5$ the value of the average SNR over the main channel is around 15dB ($\bar{\gamma}_M = 15\text{dB}$), after which the favorable fading conditions over the wiretap channel impacts beneficially the SOP metric. In addition, when $r=1.5$, the $\bar{\gamma}_M$ is shown to be around 25dB ($\bar{\gamma}_M = 25\text{dB}$). This result justifies the PLS principle how to deploy effectively the randomness of the wireless channels, i.e. fading to upgrade the system security issue.

ASC in the function of the average SNR over wiretap channel for different nonlinearity propagation cases is presented in Fig. 5. The largest ASC values are obtained for larger average SNRs of the main channel in the region of lower average SNR values of the wiretap channel. It can be noticed that by increasing the nonlinearity parameter α_E , the nonlinearity of the wiretap propagation medium decreases, and thus the ASC decreases i.e. deteriorates. In the case of $\alpha_M = \alpha_E = 2$, the results coincide with those for F fading scenario.

In Fig. 6, SPSC versus the distance ratio r for different shadowing scenarios over the main channel and different MER regimes, is illustrated. The increase in MER leads to an increase of SPSC and even equals one for $\lambda=19\text{dB}$, when the destination node is closer to the source. The SPSC dependence on the shadowing severity over the main channel is more pronounced in the range of lower MERs. For instance, for $\lambda=19\text{dB}$ the aforementioned dependence is insignificant. Further, for $\lambda=14\text{dB}$, when m_{sM} increases from $m_{sM}=1.4$ to $m_{sM}=3.4$, and $r=1.2$, the increase of less than a half order of magnitude of the SPSC can be noticed; and an increase of even one order of magnitude is noticeable for $\lambda=9\text{dB}$.

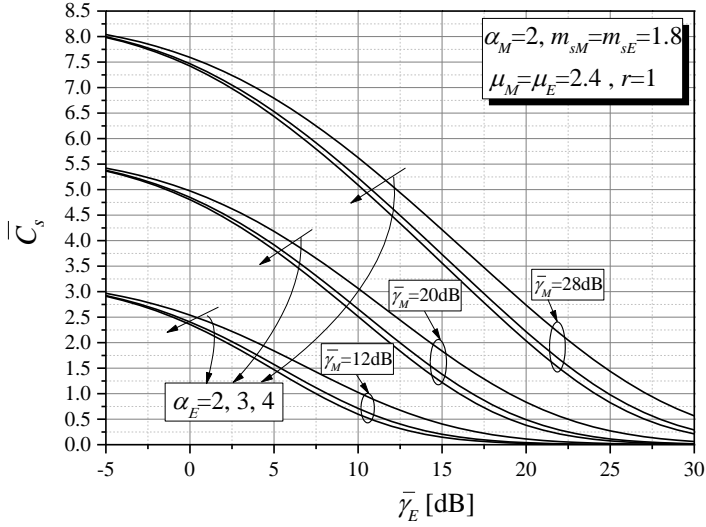


Fig. 5 ASC vs. the average SNR over the wiretap channel for different wiretap nonlinearity propagation scenarios

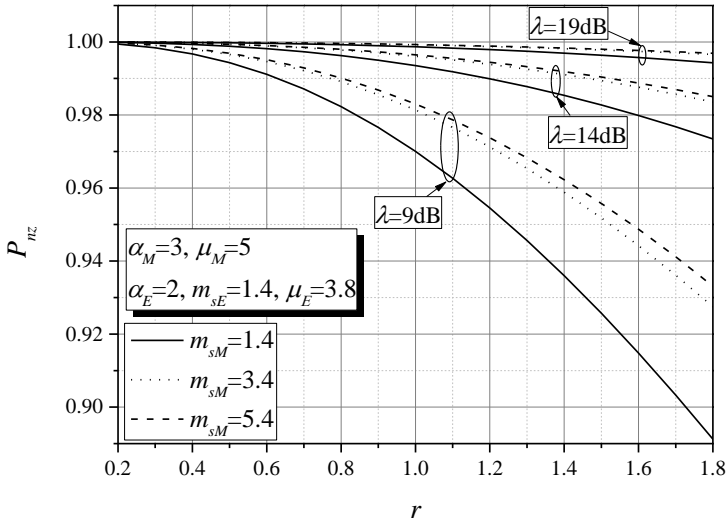


Fig. 6 SPSC vs. the distance ratio, r , for different MERs and different shadowing scenarios over the main channel

4. CONCLUSION

In the paper, the detailed analysis of basic PLS metrics over composite α - F fading channels was carried out. The obtained results showed that favorable channel conditions over main channel could upgrade the secure transmission. In addition, for i.i.d. fading channels, the impact of the fading depth, the propagation nonlinearity and the shadowing

severity depends on the space constellation of the system's nodes. Another concluding remark, assuming non i.i.d. fading channels is that the largest fading deepness over the wiretap channel assures the lowest SOP values, up to some specific value of $\bar{\gamma}_M$, and then the interplay of the same fading parameter is vice versa. This is obtained when the destination is closer to the source. Also, for the same constellation scenario, the SPSC dependence on the shadowing severity over the main channel is more pronounced in the range of lower MER values.

In overall, the obtained results can be useful in the design of securer wireless D2D communication links. Also, proposed analysis has high level of generality and can be utilized in analysis for fading scenarios which are special cases of the α - F fading model.

Acknowledgement: *This work has been supported by the Ministry of Education, Science and Technological Development of the Republic of Serbia.*

REFERENCES

- [1] W. Saad, M. Bennis, and M. Chen, "A vision of 6G wireless systems: Applications, trends, technologies, and open research problems," *IEEE Network*, vol. 34, no. 3, pp. 134–142, May 2020., doi: 10.1109/MNET.001.1900287.
- [2] B. Schneier, "Cryptographic design vulnerabilities," *Computer*, vol. 31, no. 9, pp. 29-33, Sept. 1998., do: 10.1109/2.708447.
- [3] M. Bloch, J. Barros, M. Rodrigues, and S. McLaughlin, "Wireless Information-Theoretic Security", *IEEE Transaction of Information Theory*, vol. 54, no. 6, pp. 2515-2534, 2008., doi: 10.1109/TIT.2008.921908.
- [4] R. Liu, W. Trappe, *Securing wireless communications at the physical layer*, New York, Springer, 2009.
- [5] Y. Zou, J. Zhu, X. Wang and L. Hanzo, "A Survey on Wireless Security: Technical Challenges, Recent Advances, and Future Trends," *Proceedings of the IEEE*, vol. 104, no. 9, pp. 1727–1765, 2016., doi: 10.1109/JPROC.2016.2558521.
- [6] Y. Wu, A. Khisti, C. Xiao, G. Caire, K.K. Wong and X. Gao, "A Survey of Physical Layer Security Techniques for 5G Wireless Networks and Challenges Ahead," *IEEE Journal on Selected Areas in Communications*, vol. 36, no. 4, pp. 679–695, 2018. doi: 10.1109/JSAC.2018.2825560.
- [7] A.D. Wyner, "The Wire-tap Channel," *The Bell System Technical Journal*, vol. 54, no. 8, pp. 1355–1387, 1975., doi: 10.1002/j.1538-7305.1975.tb02040.x
- [8] X. Liu, "Probability of Strictly Positive Secrecy Capacity of the Rician-Rician Fading Channel," *IEEE Wireless Communications Letters*, vol. 2, no. 1, pp. 50-53, February 2013., doi: 10.1109/WCL.2012.101812.120660.
- [9] L. Kong, H. Tran, and G. Kaddoum, "Performance Analysis of Physical Layer Security over $\alpha - \mu$ Fading Channel," *Electronics Letters*, vol. 52, no. 1, pp. 45–47, 2016., doi: 10.1049/el.2015.2160.
- [10] N. Bhargav, S. L. Cotton, and D. E. Simmons, "Secrecy capacity analysis over k - μ fading channels: Theory and applications," *IEEE Transactions on Communications*, vol. 64, no. 7, pp. 3011–3024, Jul. 2016., doi: 10.1109/TCOMM.2016.2565580.
- [11] J. M. Moualeu, D. B. da Costa, W. Hamouda, U. S. Dias and R. A. A. de Souza, "Physical Layer Security Over α - k - μ and α - η - μ Fading Channels", *IEEE Transactions on Vehicular Technology*, vol. 68, no. 1, pp. 1025-1029, 2019., doi: 10.1109/TVT.2018.2884832.
- [12] G. Pan , C. Tang, X. Zhang, T. Li, Y. Weng and Y. Chen, "Physical-Layer Security Over Non-Small-Scale Fading," *IEEE Transactions on Vehicular Technology*, vol.65, no.3, pp. 1326 – 1339, 2016., doi: 10.1109/TVT.2015.2412140.
- [13] H. Lei, I. S. Ansari, C. Gao, Y. Guo, G. Pan, and K. A. Qaraqe, "Physical Layer Security over Generalised-K Fading Channels," *IET Communications*, vol. 10, no. 16, pp. 2233–2237, 2016., doi: 10.1049/iet-com.2015.0384.
- [14] H. Zhao, Y. Liu, A. Sultan-Salem and M. -S. Alouini, "A Simple Evaluation for the Secrecy Outage Probability Over Generalized-K Fading Channels," *IEEE Communications Letters*, vol. 23, no. 9, pp. 1479-1483, Sept. 2019., doi: 10.1109/LCOMM.2019.2926360.

- [15] J. Sun, X. Li, M. Huang, Y. Ding, J. Jin and G. Pan, "Performance Analysis of Physical Layer Security over k - μ Shadowed Fading Channels," *IET Communications*, vol. 12, no. 8, pp. 970-975, 2018., doi: 10.1049/iet-com.2017.1268.
- [16] S. K. Yoo, S. L. Cotton, P. C. Sofotasios, M. Matthaiou, M. Valkama and G. K. Karagiannidis, "The Fisher-Snedecor F Distribution: A Simple and Accurate Composite Fading Model," *IEEE Communications Letters*, vol. 21, no. 7, pp. 1661-1664, July 2017., doi: 10.1109/LCOMM.2017.2687438.
- [17] O. S. Badarneh, P. C. Sofotasios, S. Muhaidat, S. L. Cotton, K. Rabie, and N. Al-Dhahir, "On the secrecy capacity of Fisher-Snedecor F fading channels," in *Proc. 2018 14th International Conference on Wireless and Mobile Computing, Networking and Communications (WiMob)*, 2018., doi: 10.1109/WiMOB.2018.8589137.
- [18] L. Kong and G. Kaddoum, "On Physical Layer Security over the Fisher-Snedecor F Wiretap Fading Channels," *IEEE Access* vol. 6, pp. 39466-39472, 2018., doi: 10.1109/ACCESS.2018.2853700.
- [19] O. S. Badarneh, "The α -F Composite Fading Distribution: Statistical Characterization and Applications," *IEEE Transactions on Vehicular Technology*, vol. 69, no. 8, pp. 8097-8106, 2020., doi: 10.1109/TVT.2020.2995665.
- [20] I. S. Gradshteyn, I. M. Ryzhik, *Tables of Integrals, Series, and Products*, fifth edition, New York, Academic Press, 1994.
- [21] The wolfram functions site, [Online] URL: (<http://functions.wolfram.com>)
- [22] V. S. Adamchik, O. I. Marichev, "The Algorithm for Calculating Integrals of Hypergeometric Type Functions and Its Realization in Reduce System," *ISSAC'90 Conference Proceedings*, Tokyo, Japan, pp. 212-224, Tokyo, Japan, 1990.
- [23] A. P. Prudnikov, Y. A. Brychkov, and O. I. Marichev, *Integral and Series: Volume 3, More Special Functions*, New York: CRC Press Inc, 1990.
- [24] A.M. Mathai, R.K. Saxena and H.J. Haubold, *The H-Function: Theory and Applications*, first edition, Springer Science, New York, 2009.
- [25] J.A. Anastasov, N. M. Zdravkovic, and G.T. Djordjevic, "Outage Capacity Evaluation of Extended Generalized-K Fading Channel in the Presence of Random Blockage," *Journal of Franklin Institute*, vol. 352, no. 10, pp. 4610-4623, 2015., doi:10.1016/j.jfranklin.2015.07.008.

CIP - Каталогизacija u publikaciji
Narodna biblioteka Srbije, Beograd

62

FACTA Universitatis. Series, Automatic Control and Robotics /
University of Niš ; editor-in-chief Marko Milojković. - Vol. 7, no. 1
(2008)- . - Niš : University of Niš, 2008- (Niš : Atlantis). - 24 cm

Dostupno i na: <http://casopisi.junis.ni.ac.rs/index.php/FUAutContRob>. -
Tri puta godišnje. - Delimično je nastavak: Facta Universitatis. Series: Automatic
Control and Robotics = ISSN 0354-2009. - Drugo izdanje na drugom medijumu:
Facta Universitatis. Series: Automatic Control and Robotics (Online) = ISSN 1820-6425
ISSN 1820-6417 = Facta Universitatis. Series: Automatic Control and Robotics
COBISS.SR-ID 158108940

